The Hebrew University of Jerusalem
Faculty of Science
The Racah Institute of Physics

Thesis submitted in partial fulfillment of the requirements
for M.Sc degree

Particle Identification via Track Imaging in Liquid-Scintillator-Core Capillary Arrays

By Michal Asher (Brandis)

Supervised by: Dr. Mark Goldberg, Soreq NRC, Yavne, Israel
And Pr. Eliahu Friedman, The Hebrew University of Jerusalem

May 2008

Acknowledgments

Of the many people who helped in this project, I owe the most to my advisors: Dr. Mark Goldberg of Soreq NRC and Prof. Eliahu Friedman of the Hebrew University of Jerusalem. I thank them for their guidance and remarkable patience throughout all stages of our work. I have learnt a lot from them, and still have a lot to learn.

I thank Dr. David Vartsky, a key member of the Soreq group, who contributed to so many aspects, major and minor.

A lot of credit is due to Dr. Igor Kreslo from Laboratory for High-Energy Physics, University of Bern, Switzerland. Igor refurbished the entire equipment used in the Bern experiment: the detector housing, the readout system and the filling system. He played a leading part in planning and performing that experiment and the results could not have been achieved without him.

My thanks are expressed to all members of the Soreq group, who contributed to this project by listening and giving good advice, if not in a more direct manner:

To Doron Bar and Dr. Gennadi Feldman, for help in the GEANT4 installation and the use of C++.

To Ilan Mor, who helped with the readout and taught me many things around the lab.

To Dr. Israel Mardor, who performed the prior simulations, some of which are quoted in this work, as well as giving valuable advice on my own simulations.

To our experienced technicians, Shaul Levy and Zion Vagish, for their assistance with the technical aspects and many good ideas.

I would also like to thank Dr. Volker Dangendorf and Ronald Lauck of PTB- Braunschweig, whose measurements of scintillator light decay times are quoted here. These measurements have proven certain things that were only at the level of plausible assumptions before I saw their data.

My colleagues and I from Soreq NRC and Bern University are indebted to the Transportation Security Laboratory (TSL) of the U.S. Dept of Homeland Security (DHS) and our project referees there, Drs. Ronald Krauss and Curtis Bell, for Risk-Reduction Research Contract No. HSTS04-05-R-RED108, under which this project was performed.

My greatest thanks go to my husband Omer, who helped and encouraged me from the first day. Your support has played a major role in this thesis, and I am more grateful than I can express.

Particle identification via track imaging in liquid-scintillator-core capillary arrays

This work describes the development of a high-spatial-resolution detector for an explosives detection system (EDS) that is based on the method of gamma resonance absorption (GRA) in ^{14}N. Apart from its imaging capabilities, the main requirements of such a detector are: high nitrogen content and the ability to distinguish, on an event-by-event basis, between internally produced protons and electrons / positrons.

The segmented detector comprises a glass capillary matrix (capillary diameter ~20µm) filled with a nitrogen-rich, high-refractive-index liquid scintillator. Gamma rays incident on the detector can create 1.5 MeV protons via the nuclear reaction ^{14}N(γ,p)^{13}C if they impinge on ^{14}N nuclei at the resonant energy of 9.17 MeV; Off-resonance gamma rays create only electrons and positrons via atomic interactions. All secondary charged particles generate scintillation light emission during the slowing down process in the active detector medium. When the index-of refraction of the liquid core is higher than that of the glass matrix cladding, part of this light will be trapped in the capillary in which it was created, providing spatial information about the point of interaction. The array face is attached to an optoelectronic readout that amplifies the signals and displays the track projection.

Differentiation between particle types is based on the difference in stopping power between proton and electrons / positrons. The latter create tracks that can be up to a few centimeters long, while the protons in question generate much shorter tracks of only ~50 µm. Furthermore, protons produce much more light per unit length along their tracks. Thus, they give rise to intense light pulses in one or two adjacent capillaries. These are very distinct from the long, faint tracks left by electrons and positrons.

The work encompassed three parts: a) development of a suitable scintillator; b) a preliminary experiment and c) Monte-Carlo simulations. The scintillator cocktail developed was based on 1-Methyl-Naphthalene. A preliminary experiment was conducted in which the capillary array was irradiated by gamma rays and neutrons from ^{137}Cs and ^{239}Pu/Be sources to study the tracks they induce. The results are encouraging and will be presented. Simulations of the detector were carried out with the Geant4 code. In these simulations, the interactions, tracks and energies of protons, electrons and positrons (including secondaries, tertiaries, etc.) within the detector are followed, in order to quantify the ratio between electron background noise and proton events.

Table of contents

Framework

The material presented in this thesis describes a preliminary proof-of-principle study towards a particle detector that is based on a micrometric glass capillary array filled with nitrogen-rich liquid scintillator. Such a detector is being developed at Soreq NRC to permit discrimination between internally-produced protons and electrons on the basis of their characteristic track lengths. It constitutes a central part of the R&D program on the Gamma Resonance Absorption (GRA) Method for explosives detection, where the relevant process in the detector is the photo-nuclear reaction $^{14}N(\gamma,p)^{13}C$.

The work encompassed three principal tasks: developing a suitable scintillator, a first experiment and computer simulations. Accordingly, this report contains a background chapter (No. 1), three empirical chapters (Nos. 2-4) and a summary (chapter No. 5). Each of the empirical chapters describes the goals, methods and results relevant to a particular task. They are presented in chronological order of the work performed.

The study was primarily carried out at Soreq NRC, except for the experiment performed at the Laboratory for High-Energy-Physics of Bern University, within the scope of the collaboration initiated by Soreq.

The first empirical chapter (No. 2) describes theoretical and experimental investigations towards synthesizing a special-purpose scintillator suitable for use in capillaries. The theoretical aspects included a search for appropriate components by attempting to match the relevant absorption and emission spectra. The experimental part consisted mainly in testing the different cocktails in order to select the optimal one.

In chapter 3, a detailed description of the Bern experiment is presented, along with its preparatory stages. The experiment consisted in irradiating the capillary array with gamma rays and neutrons, in order to study their signal shapes and associated tracks.

Chapter 4 reports on the simulations of the detector performed with GEANT4 software. These simulations follow the interactions, tracks and energies of electrons, positrons and protons within the detector.

1 Background

1.1 Gamma Resonance Absorption (GRA)

1.1.1 Preamble

Gamma resonance absorption is an explosives detection method based on the high nitrogen content characteristic of these materials 1-5). In this method resonant radiation is detected using a nitrogen-rich organic scintillator. The detectors currently in operation are based on electron/proton event separation by means of scintillation light decay time (Pulse Shape Discrimination - PSD). In the detectors discussed in this thesis, separation of such events is based on imaging the particle track in an array of capillaries with liquid scintillator core, since the typical track length varies with particle type.

1.1.2 GRA method – General

High nitrogen density is characteristic of most explosives but not of commonly transported benign materials. The GRA method relies on this property to distinguish between them. This method is uniquely well suited to large cargo containers because it is based on highly penetrating 9.17 MeV gamma radiation.

The principle of the GRA method is that the inspected object is scanned by a beam of γ-rays, a fraction of which represent on-resonance flux at 9.17 MeV, that is capable of being absorbed by ^{14}N nuclei. Thus, in addition to the familiar non resonant atomic processes that attenuate the transmitted flux, such as Compton scattering and pair production, these γ-rays will also undergo a nuclear resonance component of attenuation that is proportional to the density of nitrogen in the line-of-sight between radiation source and detector.

By measuring the transmitted gamma flux at energies on and off resonance and normalizing appropriately, both the non-resonant and net resonant (total-nitrogen) components of gamma attenuation can be extracted, as follows:

Net resonant flux attenuation = attenuation by p-γ reaction / Non-resonant attenuation (total of: photoelectric + Compton + pair production)

All the expressions for attenuation are exponentials.

It turns out that the γ-ray source closest to the ideal is the de-excitation spectrum of the excited ^{14}N* 9.17 MeV level following proton capture via the reaction ^{13}C(p,γ)^{14}N. It occurs at proton energy of 1.75 MeV and the thick target reaction yield into 4π is calculated to be ~6x10^{-9} γ/proton. Since the lifetime of the 9.17 MeV level (5.1x10^{-18} s) is very short compared to ion stopping times (typically ~1x10^{-12} s) the emission of the gamma-ray occurs during the recoil of the excited ^{14}N nucleus, resulting in Doppler-shifting ⁶⁾ of the γ-ray. At the resonant angle θ_R = 80.66° with respect to the proton beam, the nuclear recoil energy losses that occur during emission and absorption of the γ-ray by the ^{14}N nucleus are precisely compensated by the Doppler-shifted energy component.

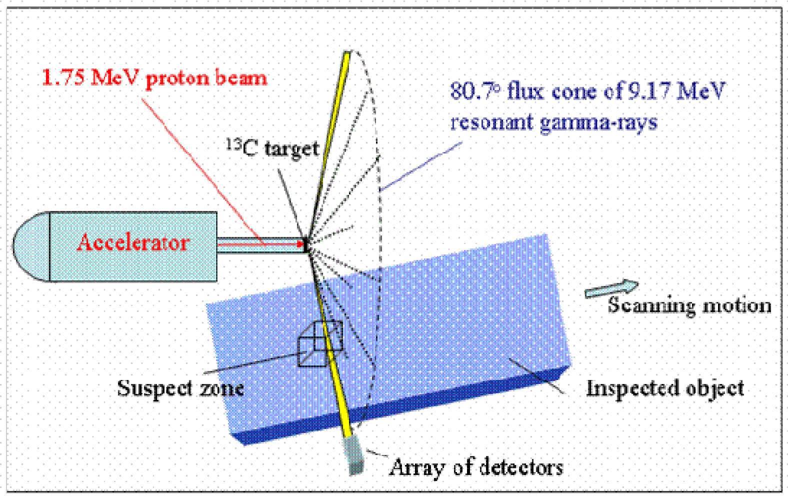

Figure 1: Schematic of GRA imaging system ⁵⁾

The GRA method is based on the photo-nuclear resonance reaction:

$$\gamma\ (9.17\ \text{MeV}) + {}^{14}\text{N}_{\text{g.s.}} \rightarrow {}^{14}\text{N}^{*} \rightarrow {}^{13}\text{C}_{\text{g.s.}}\ (0.12\ \text{MeV}) + \text{p}\ (1.5\ \text{MeV})$$

Which is the inverse of the ^{13}C (p,γ) capture reaction mentioned above.

In this reaction the nucleus ^{14}N is raised to an excited state by absorbing an incident photon. The cross section for this reaction exhibits resonant behavior and at the resonant energy of 9.17 MeV, it is ~5 times higher than the non-resonant cross section in nitrogen. When ^{14}N is excited to its 9.17 MeV state the nucleus can decay either by emission of a gamma ray or by decomposing back into ^{13}C + proton. The cross section for decomposition is 19 times larger than the cross section for decay through gamma ray emission; clearly most of the excited nuclei will undergo decomposition.

This reaction and its inverse figure in three different stages of GRA-based explosives detection: (a) in the production of 9.17 MeV gamma rays in the ^{13}C target. (b) when these gamma rays pass through the inspected object, they are attenuated by nitrogen nuclei present through this reaction. (c) within the nitrogen-rich detectors, converting the surviving resonant gamma rays into protons.

1.1.3 Bulk detectors

The PSD detectors are composed of a Pyrex vessel filled with liquid scintillator, with large (2 X 2 X 24 cm^3) dimensions [5)]. The liquid inside the vessel is a special-purpose, nitrogen-rich liquid scintillator (described in greater detail in section 1.3.2). The vessel is coupled via a parabolic Perspex light-guide to a photomultiplier tube and the entire assembly is enclosed within a light-tight cover. The 20*20 mm^2 detector face is presented normal to the γ-ray beam, forming a pixel of these dimensions.

The gamma rays interacting with the nitrogen in the scintillator give rise to the resonance response by converting ^{14}N nuclei to ^{13}C + proton. Those proton events need to be distinguished from the non-resonant electron events that also occur within the detector, due to non-resonant gamma rays and those on-resonant gamma rays that interact non-resonantly with the nitrogen component.

This event separation is realized through Pulse Shape Discrimination (PSD), a method that utilizes the relatively slow light signal produced by particles in the scintillator to separate electron events from proton events that give rise to a somewhat longer signal, spread over a wider time range. In the typical PSD spectrum displayed in Fig. 2 each peak represents different incident particles. The high, narrow peak was created by electrons (from gamma rays) and the low, broad peak is the result of knock-on protons (from fast neutrons) created by the ^{241}AmBe source. The neutrons are a good imitation of resonant photo-protons through the knock-on protons they produce in the scintillator, since these have similar energy/velocity (much slower than electrons) and their light in the scintillator has similar properties.

The principal PSD figure-of-merit employed is the ratio of the γ-peak channel height to the minimal 10-channel average in the valley between the γ and n peaks (Peak/Valley, or P/V). The normal working conditions are a fast NIM discrimination threshold corresponding to 200 keV equivalent electron energy.

In the scintillators used so far under these conditions, the P/V was ~300. In new scintillators (developed for the new detectors) the P/V is as high as 1000. More details about the new scintillator PSD properties can be found in appendix A.

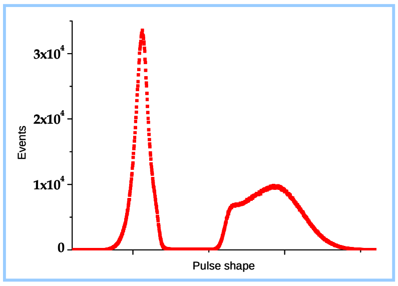

Figure 2: Typical PSD spectrum obtained using ^{241}AmBe source. The high, narrow peak is the gamma (electron) peak and the broad, low peak is the neutron (recoil-proton) peak.

These detectors combine high efficiency to energetic gamma rays with sensitive proton electron event discrimination. The new capillary array detectors were developed to achieve all these advantages, together with sub-millimeter instrumental resolution for explosives detection.

1.2 Scintillation in organic liquids

1.2.1 Properties of Organic scintillators

When a charged particle passes through matter it dissipates its energy in ionization and excitation of molecules [7,8] Some of this energy may be emitted as light, either in the visible or UV region of the electromagnetic spectrum. The process responsible for this emission is called scintillation. This emission is subsequent of molecular light absorption, usually of photon with energy higher than the energy emitted at the scintillation. This behavior is inherent of organic aromatic molecules since it follows from their electronic structure.

Scintillation can occur in vapor, liquid and solid organic phases, as long as the individual behavior of a molecule is maintained. That is, the electronic structure of a single molecule must not change because of inter-molecular forces. Thus, when the dominant inter-molecular interaction is the weak Van-Der-Waals force, the luminescent behavior of a molecule is unchanged.

The structure of organic molecules is largely determined by the electronic structure of the carbon atom that contains 6 electrons whose ground state is the $1s^2 2s^2 2p^2$ electronic configuration. However, when forming compounds, the carbon atom is excited to the $1s^2 2s^1 2p^3$ configuration, leaving 4 electrons in open sub-shells, ready to bond. These configurations allow for three possible hybridizations of the s states with the p states, which are illustrated in Fig. 3 for carbohydrates.

Both σ and π-bonds are types of covalent chemical bonds. A bond between two atoms that consists of two electrons occupying a bonding molecular orbital with cylindrical symmetry about the inter-nuclear axis is called σ-bond. A bond between two atoms that consists of two electrons occupying a bonding molecular orbital that has a nodal plane in its wave function is a π-bond. Although the π-bond by itself is weaker than the σ-bond, π-bonds are often components of multiple bonds, together with σ bonds. The combination of a π and σ-bond is stronger than either bond by itself.

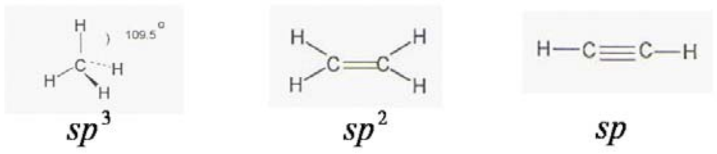

Figure 3: molecular hybridization demonstrated on hydro-carbonic molecules. A line represents a σ-bond, a double line is a π-bond and a triple line is a double π-bond.

The tetrahedral or sp^3 hybridization, in which all four electron wave functions combine to create four equivalent orbitals at 109^0 inclination to each other, (see Fig. 3) permits only σ bonds. These compounds are not luminescent.

In trigonal or sp^2 hybridization (see Fig. 3) one of the p orbitals is unchanged and three equivalent orbitals are formed. These orbitals are coplanar and symmetrical with respect to the binding axis and to the molecule plane, thus creating a σ-bond. The unchanged p orbital is symmetrical with respect to the molecular plane and can create π-bonds on top of the σ-bond already in place. The π-bonds configuration produces the hexagonal structure typical of aromatic hydrocarbons. Such compounds are luminescent, which is caused by the excited states of the π-bonds, not by the σ bond excitations.

The third form in Fig. 3 is the diagonal or sp hybridization, in which two p orbitals remain unchanged, and two equivalent orbitals are created with 180^0 between the matching σ bonds. The unchanged p orbitals create two π bonds which are luminescent.

The molecule structure is fixed by its σ bond, which create the molecular "skeleton". The π bonds and π electrons are considered to be shared along the aromatic ring. This is denoted "free electron model" since the electrons are free to move among all atoms that participate in the π-bond.

In the ground state, all orbitals are occupied by two electrons. The Pauli principle imposes that electrons being in the same orbital have opposite spins – a singlet state. For the excited states, the total spin of the molecule can be 1 or 0 and the molecule can then be in a triplet or singlet state.

The absorption spectra of molecules composed of aromatic conjugated rings contain a sequence of absorption bands in the visible and UV regions. These bands are attributed to transitions into singlet π excited states, since saturated rings, such as Cyclohexane, which contains only σ electrons, show no optical absorption at energies < 6 eV. As might be expected, the non – localized π electrons, which are less tightly bound to their parent C atoms than the localized σ electrons, require less energy for excitation.

The absorption bands display fine structure which is the result of coupling to the molecular vibrational levels. Each energy level of π electrons is superimposed with vibrational sub – levels with typical spacings of ~0.16 eV. The diagram found in Fig. 4 is typical organic molecule energy levels, including the absorption and emission bands.

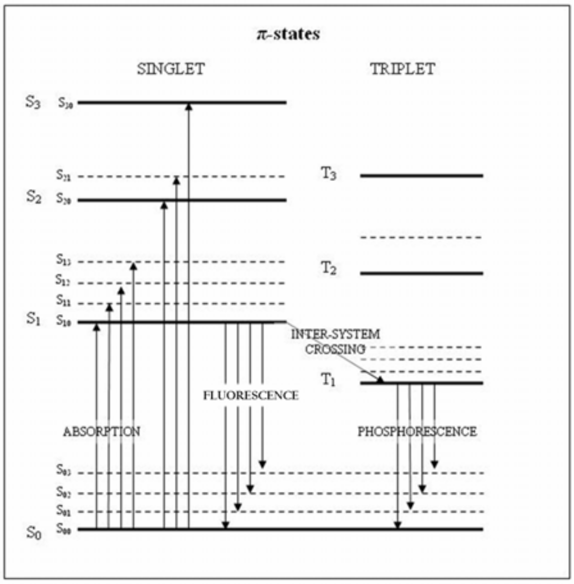

Figure 4: diagram of molecular energy levels in a typical organic molecule 7) with π bonds (such as Naphthalene, Xylene, etc.). Several of the photon decay processes illustrated are fluorescent.

The energy levels notation used in Fig. 4 the first index corresponds to the electronic energy state and the second index to the vibrational energy level.

In terms of this energy level system, the π electronic system absorption spectrum arises from transition from the lowest vibrational sub – level of the ground state S_{00} which is the predominantly populated level at normal temperature to higher energy levels such as S_{10}, S_{11}, S_{12},…, S_{20}, S_{21}, …, S_{30}, etc.

The Franck - Condon principle states that radiative electronic transitions (mainly dipolar) in the molecule occur very fast with respect to the re-adjustment time of the inter-atomic distance. Thus, in spite of similar radial dependence of the potential energy curves for different electronic levels, these curves are shifted with respect to one another as a function of the excitation energy.

So, the inter-atomic distance values corresponding to a high probability for the electron to be in the S_{00} state necessarily correspond to a low probability to be in the S_{i0} state ($i \neq 0$). As the transition probability is proportional to the square of the overlap integral between wave functions, transitions between states of the same vibrational quantum number are highly improbable.

During excitation, a π electron in the S_{00} state will be excited to a S_{ij} ($j \neq 0$) and the absorbed energy (δE_{abs}) will be larger than the energy difference (δE) between the two energy levels S_{00} and S_{i0}.

After excitation, the electron will rapidly decay to the first vibrational level by non-radiative transitions. After that, the radiative de-excitation will take place between the S_{i0} states to the S_{0j} state ($j' \neq 0$). The emitted energy (δE_{emm}) will then be lower than δE.

Finally: $\delta E_{emm} < \delta E < \delta E_{abs}$

The difference between δE_{abs} and δE_{emm} is the shift between emission and absorption spectra of a molecule which is called the Stokes shift. The Stokes shift prevents the scintillator from re-absorbing the photons it emitted. The larger the Stokes shift, the more transparent the scintillator will be to the radiation it emits.

Another important quantity is the molar extinction coefficient ε, which is defined by

$$I = I_0 10^{-\varepsilon cd} ,$$

where I_0 and I are the incident and transmitted light intensities respectively, c is the concentration of the absorbing compound in moles per liter, and d is the thickness of the specimen in cm.

1.2.2 Theory of scintillation process

There are three principal types of luminescence 7) that can occur in organic molecules: fluorescence, phosphorescence and delayed phosphorescence (Fig. 4). Fluorescence is the radiative transition from S_1 to S_0, following absorption. The radiative lifetime of S_1 is in the $\sim 10^{-8}$ s range, so the molecule reaches thermal equilibrium before emission, thus the transition occurs from S_{10} into the different vibrational levels S_{0i}. This emission spectrum sometimes overlaps the absorption spectrum. The intensity of fluorescence emission decays exponentially with time.

Phosphorescence is emission at longer wavelengths than fluorescence, and with a much longer decay time. Delayed phosphorescence is emission with an identical spectrum to fluorescence, but decays non – exponentially with a long decay period.

The origin of these two types of luminescence can be explained as due to the existence of metastable triplet state T_1 below S_1. Level T_1 is populated by internal conversion from S_1 and has a lifetime of $\sim 10^{-4}$ s and ranging up to seconds. It can decay radiatively to S_0 which is the phosphorescence. It can also acquire sufficient thermal energy to return to S_1, leading to delayed emission which is the Delayed phosphorescence.

The relevant liquid scintillators are binary and ternary component systems. The binary system is typically composed of 99%+ liquid solvent and a single solute that acts as wavelength shifter (also called phosphor). A ternary system is composed of the solvent and two solutes, the primary and secondary wavelength shifters (phosphors). The primary phosphor is the intermediate between the wavelength emitted from the solvent molecules and the wavelength absorbed by the secondary phosphor.

These phosphors are called "primary" or "secondary" by their relative concentrations. For example, in a typical ternary scintillator out of 10,000 molecules 9900 will be solvent molecules, 91 primary phosphor molecules, and only 9 molecules are secondary phosphor molecules.

Any fluorescent organic compound is a potential scintillator or component of a scintillating system. Its utility as a scintillator depends on such molecular properties as fluorescence and absorption spectra, quantum efficiency and decay time.

An ionizing particle transversing a scintillator will lose its energy to the scintillator, predominantly through electromagnetic interactions. In an organic liquid scintillator this means that the energy is passed to the solvent molecules which occupy 99%+ of the scintillator volume. The solvent molecules transfer their energy to the primary phosphor molecules, which later transfer their energy to the secondary phosphor molecules.

Scintillation is not responsible for the particle stopping process. Only up to ten percent of the incident particle total energy is lost to scintillation. The incident particle stopping is discussed in detail in section 1.3.3.

Fig. 5 and Table I describe the possible molecular processes inside a binary scintillator system. The energy levels structure of two solvent molecules (denoted by m in S_{1m}) and one wavelength shifter (denoted by n) molecule are illustrated. In this diagram the processes are denoted by Latin numeral, each corresponding to a process in Table I. The table is divided according to three processes classification: (a) primary processes in the solvent, (b) secondary processes in the solvent, and (c) processes in the phosphor.

The primary processes are those created directly by the ionizing particle traversing the scintillator. The main primary process leading to scintillation is process I – excitation of π electrons, mainly into the 2nd and 3rd singlet states. This is followed by V – internal conversion to level S_{1m}, in which approximately one third of the energy is lost. Of all these, the only process contributing to scintillation is process I.

Next, the solvent molecule excited to S_{1m} is subject to de-excitation processes VI – X which start competing. Out of all possible solvent de-excitation processes only fluorescence and migration to solute (radiative and non-radiative) will contribute to scintillation. Eventually, excited phosphor molecules are able to emit light in the UV or visible range. However, not all excited phosphor molecules contribute to scintillation since some undergo decay to the ground state via internal conversion.

Table I: Possible processes [7)] inside a binary scintillator system classified according to the three scintillation stages. Each is denoted by a Latin numeral representing a process in figure 5.

#	Primary processes in the solvent	#	Secondary processes in the solvent	#	Final processes
I	π- electron excitation	**V**	Internal conversion from S_{2x}, S_{3x} to S_{1X}	**XII**	Escape of the solvent emission
II	π electron ionization	**VI**	Fluorescence emission of photons, due to radiative $S_{1x} – S_{0x}$ transition, and leading to processes VIII or X	**XIII**	Primary solute emission
III	Excitation of electron other than π electron	**VII**	Internal quenching in which E_{1x} is dissipated non-radiatively	**XIV**	Internal quenching in the solute
IV	Ionization of electron other then π electron	**VIII**	Radiative migration in which the emitted photon is absorbed by another molecule of the solvent		
		IX	Non-radiative migration in which E_{1x} migrates between molecules prior to emission		
		X	Radiative transfer to a solute molecule		
		XI	Non-radiative transfer to a solute molecule		

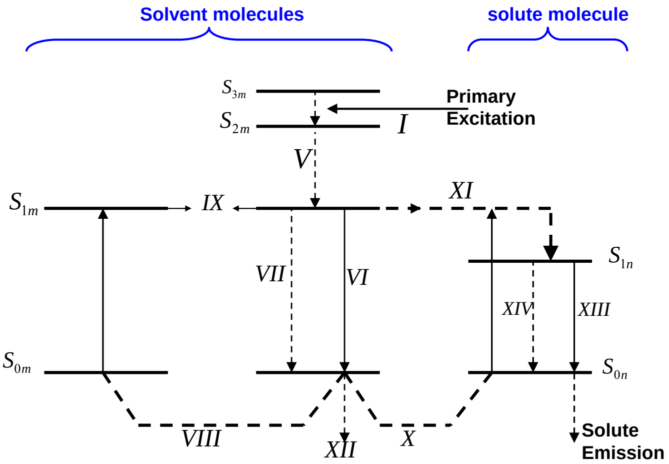

Figure 5: A diagram of processes [7)] contributing to scintillation inside a binary scintillator system. They are detailed in Table I, according to the Latin numeral that represents each.

1.2.3 Bulk detector scintillator properties

Naturally, it is of interest that the scintillator should have the maximal light yield. One of the factors governing the scintillation efficiency is that energy losses at all stages of the scintillation process, must be minimized.

The bulk detectors contained a large amount of liquid scintillator, discriminating between electrons and protons events using the PSD method (section 1.1.3). Therefore, the most important characteristic of the scintillator, in addition to high light yield, is the intensity of the long scintillation component. The conventional theory is that primary process II (π electron ionization) followed by ion recombination, yields molecules in excited triplet or singlet π–states. These excited triplet states are principally responsible for the long scintillation component.

The long component is usually also the most sensitive to impurities in the scintillator, since it is the most vulnerable to collisional quenching. The scintillator in the GRA application needs to be nitrogen rich, which is accomplished by dissolving a nitrogen-rich-additive (NRA) in the liquid scintillator base. The long component of the scintillator should not be dramatically affected by the nitrogen rich additive. In general, the base scintillator should be quench resistant and the additive molecules should ideally behave as totally passive bystanders with respect to the transfer of excitation from the solvent to the solution.

Doping with NRA imposes a further requirement on the base scintillator – it has to be capable of dissolving large concentrations of NRA.

1.3 Micrometric capillary detectors

1.3.1 Principle of operation

The new detector is made of a glass capillary array filled with nitrogen rich liquid scintillator. As in the bulk detectors, gamma rays incident on the detector can create photo-protons if they are at the resonant energy; off the resonance energy, they create electrons only. These ionizing particles cause light emission from the scintillator as they lose their kinetic energy to the liquid scintillator medium.

The track image is achieved by looking at the array face, perpendicular to the main capillary axis. This track is generated as the ionizing particle dissipates energy in all the capillaries it transverses.

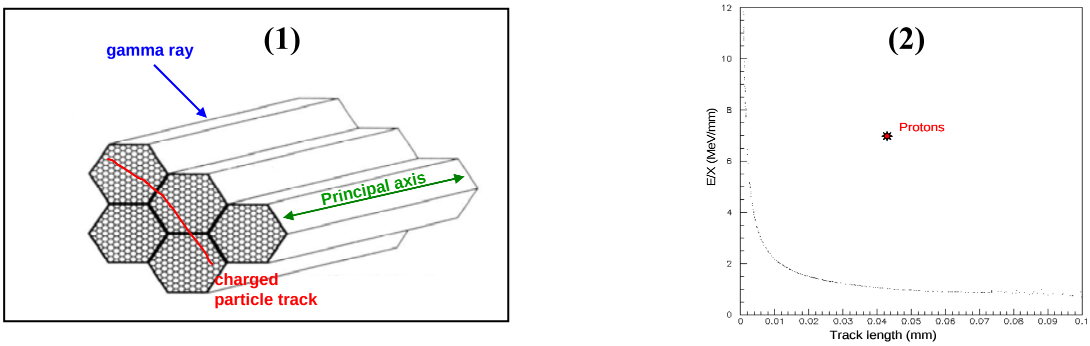

Figure 6: (1) schematic illustration [9] of capillary detector operation principle. A gamma ray can create light anywhere along a capillary, of which a certain portion will reach the capillary face. (2) E/X vs. electron track length (curve) and 1.5 MeV protons (large dot) [5]

Discrimination between particle types in the new detector is based on the difference in track length and overall light intensity between slow and fast charged particles. Light charged particles, such as electrons and positrons, create tracks that are centimeters long while protons give rise to much shorter tracks, only ~50 µm for 1.5 MeV protons. However, protons leave much more light per unit length along their tracks than electrons. Thus, protons show strong bursts of light over a short trajectory, typically a single capillary, which are very distinct from the long, fainter tracks of electrons.

1.3.2 Capillary detector scintillator properties

The most important figure-of-merit in the capillary detector scintillator is the light output at the end of each capillary. In order to maximize it, the scintillation yield is not the only factor – high refractive index, high optical transparency of the scintillator and a large Stokes shift between the absorption and the emission spectra are all important. These factors will now be discussed.

The refractive index of the liquid scintillator (see section 1.3.4) should be as high as possible in order for the critical angle of total internal reflection to be as large as possible, allowing a greater portion of the light to reach the end of the capillary. This portion is a small fraction of the total light yield, typically 5%-15%, so that the refractive index is just as important in such detectors as the overall light yield. Since the solvent constitutes 99%+ of the base scintillator, it thus determines the refractive index.

High optical transparency and large Stokes shift make the scintillator transparent to the radiation it emits. The Stokes shift relates to the case where the photon is re-absorbed by a molecule of the same species it was emitted from. High optical transparency related to the case in which the photon is re-absorbed by any other molecule. This means, in technical terms, that the solvent should be clear and the wavelength shifter utilized must not color the solution.

The probability that a photon will be re-absorbed is important not just to the light output at the end of each capillary, but also to the localization of the track. If a photon emitted in a capillary is re-absorbed in a neighbor capillary, it may cause emission in that capillary, thus creating more light at the end of the neighbor capillary end as well.

Most of the requirements from the nitrogen-rich-additive (NRA) remain unchanged from the bulk detectors: (1) the light yield of the base scintillator should be minimally affected by the NRA. (2) The scintillator cocktail should be capable of dissolving large concentrations of NRA.

1.3.3 Interactions in the scintillator

Electromagnetic radiation interacts with the absorber, in this case mainly the scintillator, in single events. The interactions via which the energy is transferred to the scintillator depend on the incident gamma energy. Since the special-purpose scintillator inside the capillaries is nitrogen rich, resonant gamma rays can undergo the nuclear resonant reaction discussed in 1.1.2, producing 1.5 MeV protons and ^{13}C atoms.

Non-resonant gamma rays interactions[9-11)] that can occur are:

i. Compton scattering
ii. Photo-electric effect
iii. Pair production

The fraction f of the incident quanta which are absorbed, i.e., undergo one (or more) of these interactions, in their passage through a scintillator of thickness d is:

$f = 1 - e^{-\mu d}$

$\mu = \sigma + \tau + \chi$

μ- Linear attenuation coefficient, in cm^{-1}.

σ, τ, χ - Linear attenuation coefficients for Compton, photo-electric and pair production, respectively.

Each of these coefficients depends on the energy of the electromagnetic radiation and on the nature of the absorber. At ~9.17 MeV in organic scintillators τ is essentially negligible, χ is more significant but still relatively low in comparison to σ, thus determining that Compton scattering is the dominant interaction at this energy.

In Compton scattering and pair production, which are the relevant interaction processes for non-resonant gamma rays, the secondary charged particles created are free electrons and positrons at various energies.

All primary particles – electrons, positrons and protons, leave kinetic energy in the active medium they traverse through a sequence of ionizations and excitations. But, whereas electrons and positrons at this energy are minimum ionizing particles, protons are much slower and their specific energy loss dE/dX is much higher.

A proton incident on a scintillator dissipates its energy predominantly in a succession of inelastic collisions with the constituent electrons, resulting in molecular excitations and ionization. The proton path in the scintillator is essentially straight (apart from the rare event of a nuclear collision, when large angle scattering occurs) as the momentum transfer in these collisions is relatively small.

An electron in its passage through matter dissipates its energy in excitation and ionization, and is scattered in collisions with electrons and nuclei. Energy can also be dissipated as radiation (Bremsstrahlung), but this effect is proportional to Z^2, where Z is the atomic number of the absorber and has linear dependence in E. In organic compounds Z is low so the effect is negligible at energies <10 MeV.

In its interactions with the matter, the electron may undergo appreciable deflections, so that its path through the scintillator at energies up to ~10 MeV is not straight but tortuous. Hence the concept of range in a material is different for protons and electrons. What was defined as range for protons is the projected range for electrons; unlike protons, the range of electrons is an empirical quantity corresponding to the thickness of absorber required to stop most of the electrons at a given energy.

The range of positrons in a material is similar to that of electrons. At the end of its range however, a positron interacts with an electron in the absorber, and the rest mass of the two particles is annihilated and converted into electromagnetic annihilation radiation of total energy

$2m_0c^2 = 1.02$ MeV ,

m_0 being the electron/positron rest mass. The annihilation radiation consists predominantly of pairs of quanta, each of energy 0.51 MeV, emitted in opposite directions. The absorption of this electromagnetic radiation was already discussed at the beginning of this section.

Energy required for molecule excitation to fluorescent energy level is only a few eV, much lower then incident particles energies, 1.5 MeV for protons and up to ~9 MeV for electrons. The primary proton or electron can transfer energy directly to molecule excitation or by ionizing a molecule, creating a secondary electron of lower energy that will transfer its energy to molecular excitation. Several generations of such electrons can be produced and contribute to the fluorescent excitation process. The electron generations created by the secondary electron and on are called "delta electrons".

These secondary and delta electrons cause track branching and broadening. The branching is more common in primary electron tracks than in proton tracks, whereas the widening is common in both. The broadening has an effect on track shape only if, on average, it is larger then a capillary radius. In the chapter dealing with simulations of the capillary array theoretical such tracks can be seen, for example in Fig. 32, chapter 4.

The number of protons is the interesting factor, since each photo-proton is the result of a single resonant photon. Counting the protons allows determination of nitrogen content in the inspected object. Proton events need to be discriminated from electron and positron events in order to detect nitrogen in quantitative manner.

1.3.4 Light collection in capillaries

The light emission in the scintillator is followed by propagation of this light through the capillaries. A key property of the capillary structure responsible for this propagation is the refractive index, effecting on the fraction of light going through total internal reflection [9,13,14)].

Refractive index is a quantity that represents the velocity at which an electromagnetic wave travels inside a medium. It is a result of the interaction between the electromagnetic wave and the material's molecules. A somewhat schematic view of this problem is as follows: the incoming electromagnetic field polarizes the medium molecules, creating a field of oscillating dipoles. Then the oscillating electrical charges cause new electromagnetic radiation to be emitted. A simplistic calculation of the refractive index 15) relates to the molecule behavior only as a result of the incoming electromagnetic wave. A more sophisticated calculation also takes into account how the dipole field created by the oscillation of the surrounding molecules affects each molecule.

A photon, incident upon the interface between two transparent optical materials having different indices of refraction, will be totally internally reflected (rather than refracted) if:

1. The photon is incident upon the interface from the high refractive index medium and;

2. The angle of the photon relative to the normal to the interface is greater than some critical angle, the latter being dependent only on the indices of refraction of the media.

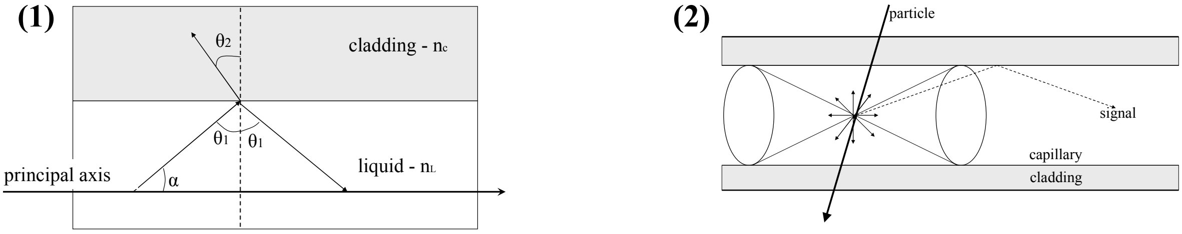

Figure 7: optical geometry. (1) Angles at the interface between liquid and cladding; (2) The fraction of light moving along a capillary 9)

The angle of reflection is equal to the angle of incidence. By definition, the angle is measured between the incident ray and the normal to the interface at the point of reflection. Light is transmitted down the length of a capillary at a constant angle to the capillary principal axis. In passage between two materials, the relationship between the angle of incidence θ_1 and the angle of refraction θ_2 is expressed by Snell's law (depicted in Fig. 7(1)):

$n_L \sin \theta_1 = n_C \sin \theta_2$
n_L - the liquid core index of refraction
n_C – the (glass) cladding index of refraction

In other words, total internal reflection will only take place if the refractive index of the liquid scintillator used as core is higher then the refractive index of the glass capillary used as cladding. The difference between the two indices should be as large as possible, in order to allow as large a fraction as possible to be internally reflected.

In order to calculate the critical (maximal) angle for total internal reflection, we have to take $\theta_2=90^0$, and then:

$\sin\theta_{crit} = n_L/ n_C$

Scintillation light is emitted isotropically in all directions. Only the light inside the cone determined by the critical angle will be reflected along the capillary – see Fig. 7(2). The formula for calculating the trapping efficiency ε is based on the solid angle of the light cone:

$$\varepsilon = \frac{1}{2}\left(1 - \frac{n_C{}^2}{n_L{}^2}\right)$$

Thus for glass cladding (n_C = 1.49) and with our best performing liquid scintillator (n_L = 1.617), ~9% of light will contribute to the signal at each capillary end. But as the quality of an individual capillary is far from perfect and their shape not cylindrical but somewhat hexagonal, the real value will be closer to 16):

$$\varepsilon_m = \frac{1}{2}\left(1 - \frac{n_C}{n_L}\right)$$

This is calculated in an approximation that considers only meridional rays – rays that pass along the principal axis. For the same values of scintillator and cladding refractive indices the fraction of light reaching each capillary end will be ~4.6%. Therefore, considerable effort was put into maximizing the light yield of scintillator and its refractive index.

An off-axis ray of light traversing a capillary 50 microns in diameter may be reflected 100 times per centimeter of capillary length. This number is inversely proportional to the diameter. Total internal reflection between two transparent optical media results in a loss of less than 0.001 percent per reflection 16); thus an appreciable quantity of light can be transported several tens-of-centimeters along a capillary without encountering severe losses.

Scattering from the true geometric path can occur, however, as a result of attenuation in the liquid scintillator core and irregularities in the core/cladding interface. In both cases, light will be scattered in proportion to capillary length, depending upon the angle of incidence. To be functional, therefore, long capillaries must have an optical quality superior to that of short capillaries.

1.3.5 Spatial resolution

Instrumentally, the resolution is determined by the diameter of the constituent capillaries. The entire array is a matrix divided into pixels, a pixel being defined by a single capillary. The narrowest capillaries available are 10 μm in diameter, that is therefore the upper limit on the resolution.

The spatial resolution is also determined by the optical readout system, but in practice the limit was set by the capillaries diameter.

There are several factors that cause the resolution to be degraded. First, the amount of light traversing through the cladding into adjacent capillaries will cause decrease of the signal in the relevant capillaries and an increase of noise in the adjacent ones. In order to minimize this effect, Extra-Mural-Absorbers (EMU) should be placed between the capillaries, preferably integrated into the capillary matrix.

The glass partition between capillaries has a thickness of ~11 μm for the 20 μm capillary diameter array (which incorporates EMU's and is better suited for our purpose) used in the Bern experiment. This thickness needs to be taken into account when considering the spatial resolution.

In addition to the instrumental constraints, the spatial resolution achievable is also limited by the track properties of the secondary ionizing particles. For protons, once a proton divides its energy between two capillaries the light produced at each capillary may not be intense enough and the event may be mistaken for an electron event. For electrons, under certain conditions, insufficient energy may be deposited in some of the capillaries to be detected, thus creating an intermittent track.

1.4 Monte Carlo simulations

Monte Carlo methods are a common way to simulate physical systems [17,18)]. They invoke a computational algorithm based on repeated random sampling to compute the desired quantities. Monte Carlo methods are most useful when it is logistically unfeasible or impossible to compute an exact result by means of a deterministic algorithm.

GEANT - GEometry ANd Tracking - is the name of a series of simulation codes designed to describe the passage of elementary particles through matter, using Monte Carlo methods. Originally developed at CERN for high energy physics experiments, today GEANT has been put to use in other fields, by variety of contributors.

Geant4 is the latest version in the GEANT series of software toolkits and the first to use C++ - object-oriented programming. Its development, maintenance and user support are provided by the international Geant4 Collaboration. At the core of Geant4 is a set of physics models to represent the interactions of particles with matter across a broad energy range.

Geant4 incorporates facilities for handling geometry, tracking, detector response, run management, visualization and user interface.

The following is a brief outline of each of the above facilities:

- Geometry is the physical layout represented by the simulation, including all objects such as detectors, absorber, etc.
- Tracking simulates the passage of a particle through matter. This involves considering possible interactions and processes.
- Detector response evaluates (within certain approximation) how a real detector would respond to particle transversing its volume.
- Run management records the details of each simulation run.
- Geant4 offers a number of options for visualization, including OpenGL, and a user interface based on command-line.

Writing a simulation is basically divided into three main parts. First the "physical" system has to be defined: including materials, sizes, geometry, etc. for the online representation of all objects. Second, the "physics list" to be simulated has to be defined, including particle types and the processes these particles can undergo. Third, an event that triggers the simulation, such as a proton with certain energy and direction has to be defined.

2. Special-purpose scintillator development

2.1 Preamble

The scintillator utilized in the micrometric capillary array detector has a very different function from that of the scintillator previously used in the GRA application using bulk detectors. The requirements from the new scintillator are discussed in detail in section 1.3.2. The desired principal characteristics of the new scintillator are: high light yield, high refractive index, optical transparency, large Stokes shift, quench resistance and a good solvent.

The development and optimization of the special-purpose, nitrogen rich, high-refractive-index scintillator involves a tradeoff between the different requirements in order to reach the composition that is most suitable for the application.

The development program included:

(a) A theoretical study that included a search for all candidate materials for producing the desired scintillator.

(b) After acquiring as many candidate materials as possible, the different emission spectra of the solvents were compared with the phosphors absorption and emission spectra to find the best theoretical matches, in terms of maximal spectral overlap 19).

(c) Then, the light yield of all the solvent was measured with the phosphor that appeared to be most appropriate, in order to choose the best solvent.

(d) After the solvent had been chosen, different phosphor combinations were tested, and the optimal composition of the scintillator cocktail (without nitrogen) was determined.

(e) In the final stage, small amounts of nitrogen rich additive were added to test its solubility.

A full list of materials investigated including full names and details can be found in appendix D.

2.2 Candidate materials

This task included the search for all scintillator components including solvents, primary and secondary phosphors. Over and above the basic components, several options were considered for additives that might increase the refractive index or the light yield of the scintillator. The nitrogen rich additive, however, was known to begin with.

2.2.1 Solvents

The base for every liquid scintillator is the solvent, which constitutes ~99%+ of its quantity. Hence, it determines the refractive index of the entire scintillator. Thus, in the first stage of the search the principal criterion for a solvent was its refractive index. A literature search yielded the following list of candidates:

Table II: list of solvents [9,20)] and their principal spectral characteristics. For full chemical names and more data see appendix D

Solvent	Absorption peak (nm)	Emission peak (nm)	Refractive index
1-MethylNaphthalene (1MN)	282	340/323	1.617
2-MethylNaphthalene (2MN)	276	335/320	1.604
1-PhenylNaphthalene (1PN)	288	345	1.666
p-Xylene	275	290	1.49

2MN is a solid isomer of one of the principal solvent candidates, 1MN. 2MN can be dissolved in 1MN, to an extent that a solution dominated by 2MN can be achieved. This solution may be a better basis for a scintillator than pure 1MN.

p-Xylene is the solvent employed in the bulk detectors. It has low refractive index and is therefore ill-suited to the capillary array detector.

2.2.2 Phosphors

With respect to phosphors, it is hard to predict the light yield of a cocktail containing them in advance. The principal theoretical tool at hand is spectral investigation of cocktail potential ingredients. This study is explained in detail in the next section (section 2.3).

All available scintillators were collected and tested. A literature search has produced several promising candidates that had to be ordered, and candidates that were already available were tested as well. Table III lists all these phosphors, with each phosphor peak emission and peak absorption.

Table III: list of tested primary and secondary phosphors, including mean spectral maxima.

Phosphors	**Absorption peak (nm)**	**Emission peak (nm)**
PPO	310	358
Di-Methyl-POPOP (DMPOPOP)	365	420
POPOP	355	420
OG-408	346	387
OG-426	360	440
TPB (three suppliers)	340	435
bis-MSB	347	420
α -NPO	335	395
p-Quaterphenyl	300	380
PPD	280	340

2.3 Theoretical spectra analysis

A promising theoretical approach for obtaining high light yield efficiency is to compare the emission and absorption spectra of cocktail ingredients. These spectra can usually be found in the literature 19). Most spectra are available fully, but for OG408only selected values such as location of peaks were found21). The presentation format for the spectra is typically as follows: The absorption and fluorescence curves are presented together in a single figure. The fluorescence spectrum represents relative photon flux per wavelength and the absorption curve represents the molar extinction coefficient (defined in section 1.2.1) in liters mole^{-1} cm^{-1} versus wavelength. Most curves were measured using Cyclohexane as solvent.

Absorption and emission spectra of cocktail components for home made scintillator are presented in Fig. 8. Spectra presented are the solvent – 1MN, three candidates for main phosphor – bis-MSB, OG408, POPOP and a candidate for secondary phosphor – PPO. All spectral curves are presented in full, except for the spectra of the leading candidate OG408 which is presented in a partial manner, as can be found in literature 19) The lines represent the peaks of emission and absorption, both in their location and relative intensity. It is clear that the spectral curves of OG408 should be continuous; therefore straight lines have been drawn between the peaks, to allow a rough estimate of the curve shape.

The spectral intensity in all the graphs is represented in the wavelength range of 200 – 500 nm, with the wavelength increasing from right to left (the energy increases in the opposite direction). Consequently, the curve on the right is the absorption (abs) and the one onto the left is the emission spectrum (em).

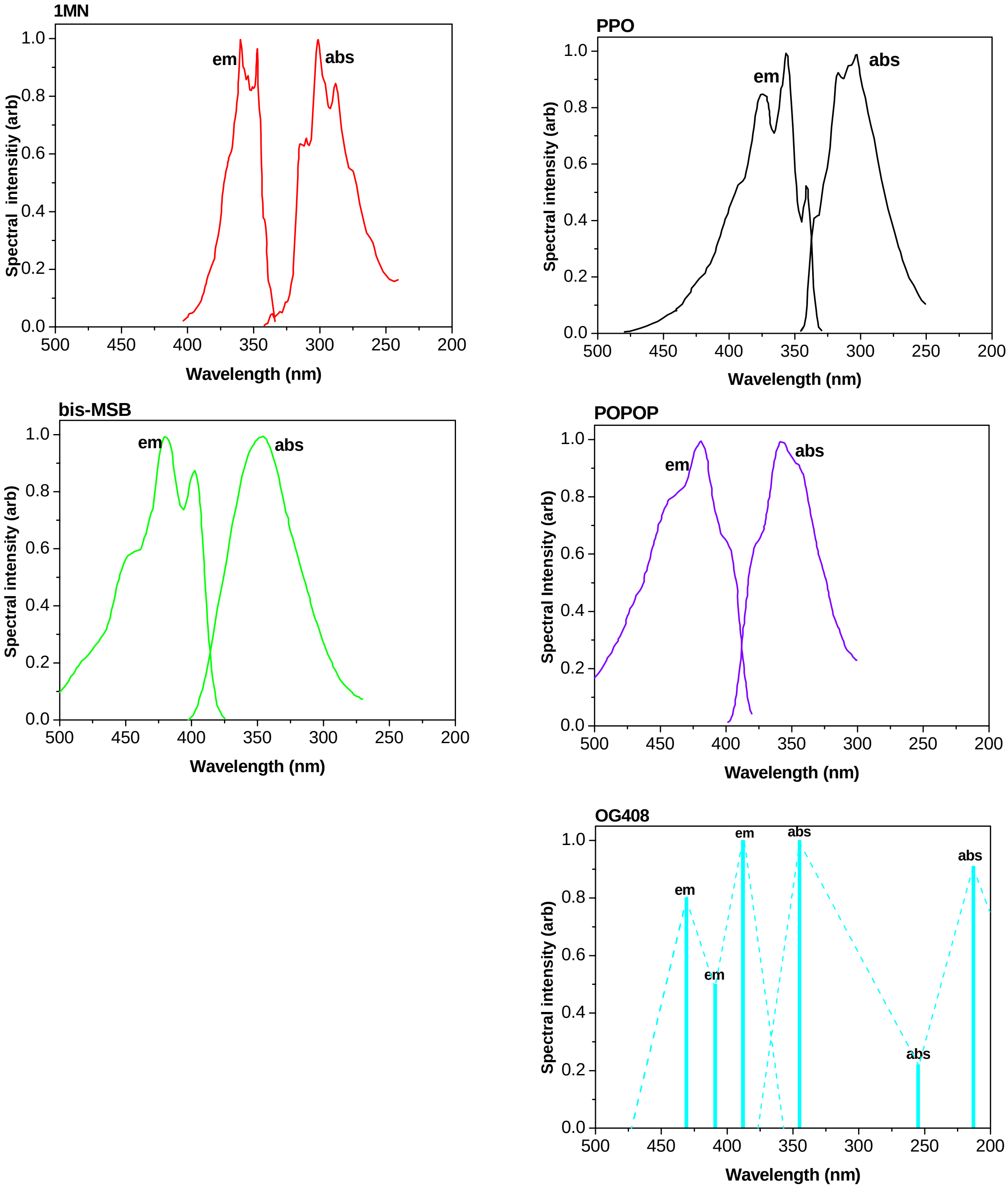

Figure 8: absorption and emission spectra of 1MN (solvent), bis-MSB, OG408, POPOP (primary phosphors) and PPO (secondary phosphor). The spectra represent detailed experimental data for all 19) but OG408, for which such data exists only for peak location and relative intensity 22). The full spectra in this graph are linear approximation, and the peaks locations are marked.

The solvent, all three secondaries and the primary phosphor are all in the same spectral region. It seems all cocktail combinations are practical. In order to examine cocktails spectral match in more detail the curves should be placed on the same graph.

The cocktails investigated in this research were either binary or ternary. Binary cocktails are composed of solvent with one phosphor. In ternary cocktails there are two phosphors, primary and secondary. Both cases are hereby discussed.

2.3.1 Binary cocktail

The spectral behavior of the binary cocktail is easier to understand, since fewer energy-transfer processes are involved than in ternary scintillator cocktails. As discussed in the theoretical background (sec. 1.2.1), the solvent molecules will absorb the energy of a particle passing through the scintillator (either directly or through electromagnetic processes).

The absorption spectral curve of the phosphor should overlap to as large an extent as possible the emission curve of the solvent, so that the phosphor molecules can efficiently absorb the light emitted by solvent molecules. By this criterion, greater spectral overlap between the solvent emission and the phosphor absorption should therefore lead to higher scintillation efficiency.

The first example of good spectral overlap is 1MN combined with OG408 (Fig. 9). The 1MN emission curve and OG408 absorption curve overlap very well. Experimental results (section 2.5) show that this cocktail has the highest light yield of all candidates. The reason for high light yield in this case could be that the absorption curve of OG 408 is very wide, so it is capable of absorbing photons over a much broader range of wavelengths than other phosphors.

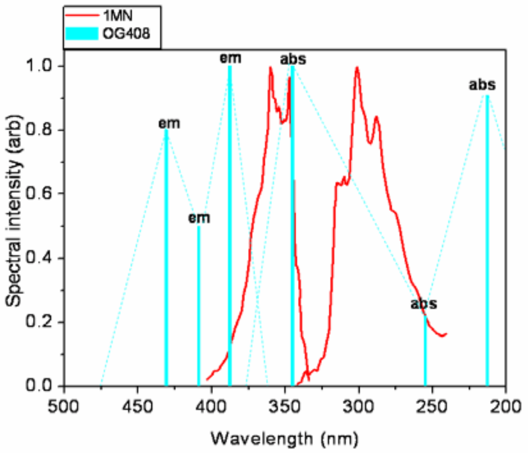

Figure 9: Spectral intensity of binary scintillator cocktail containing 1MN + OG408, cocktail with best light yield.

Fig. 10 enables comparison between two spectra of binary cocktails. To the left, 1MN combined with POPOP and to the right, 1MN combined with bis-MSB. Both phosphors are extensively employed and known to have excellent light yield. The overlap between the emission curve of 1MN (the solvent) and both bis-MSB and POPOP absorption curve is outstanding, seemingly better than in Fig. 9.

This gives rise to the expectation that the light yields of both cocktails will be high, and perhaps even similar, according to the above-mentioned criterion. Both phosphors can collect all the light emitted from the solvent and emit it in the visible range, with peak emission at ~425 nm.

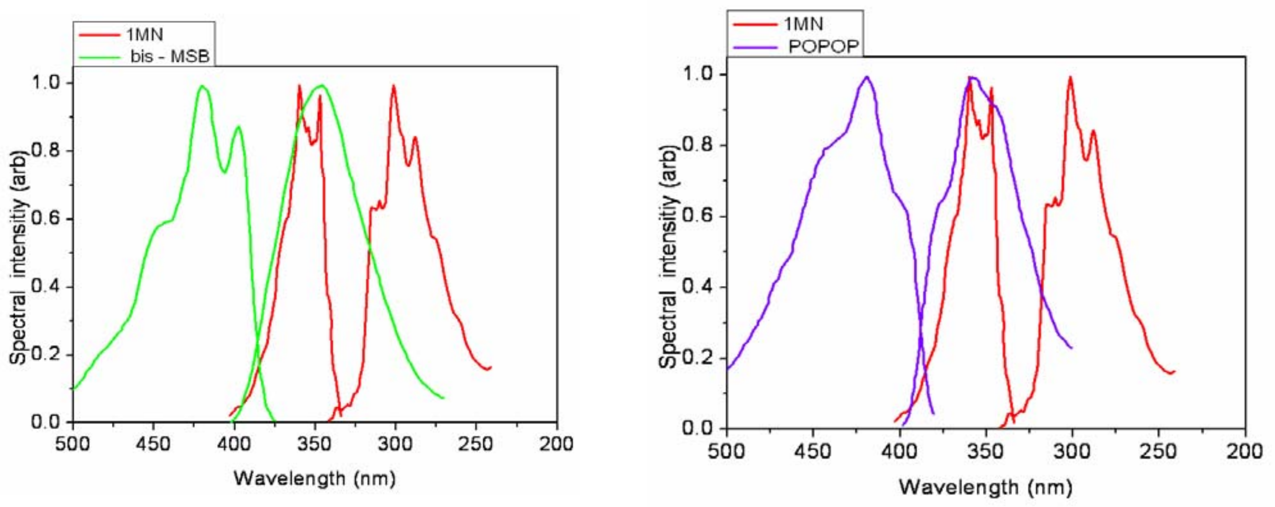

Figure 10: Spectra of two binary cocktails. To the right 1MN + bis-MSB, to the left 1MN + POPOP. The spectral overlap between the emission of the solvent and the absorption of the phosphor is excellent.

In reality, however, experimental results described in detail in sections 2.4, 2.5 show quite a different behavior. 1MN combined with bis-MSB has light yield much superior to the light yield of 1MN combined with POPOP. This can be explained, for example, by the yellowish color of the cocktail containing POPOP, suggesting some re-absorption in the solution. Another possibility is that the energy transfer from solvent to phosphor molecules is poor, despite the spectral overlap criterion being rather well fulfilled. Finally, quenching processes might be dominant over radiative processes in phosphor molecular de-excitation in this solvent. There is no easy way to discover which of these explanations is correct, but clearly there is more to high light yield efficiency than mere spectral overlap.

In conclusion, spectral overlap is not a sufficient criterion to predict the light yield efficiency and all options must be experimentally tested. However, looking at the spectral curves of scintillator ingredients is educative, and does provide qualitative guidelines for predicting scintillator behavior.

2.4 Experimental setup

All measurements on scintillator samples were intensity determinations of one of the following:

(1) Total Light Yield (TLY) - the light output integrated over the entire event.

(2) Fast Scintillation Component Ratio (FSCR) – Fast component of the light output divided by the total light output.

Prior to measurement, the sample was bubbled with clean nitrogen gas for two minutes, to eliminate molecular oxygen from the solution. This is necessary since oxygen causes quenching and reduces light yield by ~10% - the effect of oxygen on light yield is further discussed in appendix B.

The experimental setup is illustrated in Fig. 11. The Hamamatsu Photomultiplier Tube model R1828-01 (PMT) has a 2" diameter photocathode and 1.3ns pulse rise time. The vial containing the scintillator sample is wrapped in white Teflon which serves as a diffusive reflector in order to improve light collection. It is attached to the PMT tube with Bicron BC630 optical grease. The PMT tube with the scintillator sample was placed inside a light-tight enclosure. Scintillation was activated using a ^{137}Cs radiation source, and the PMT was powered by a Tennelec TC953 high voltage power supply.

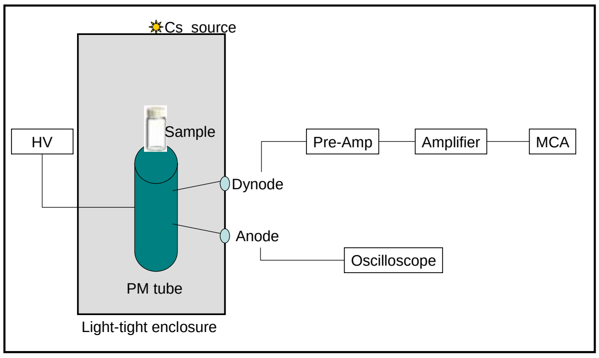

Figure 11: Schematic diagram of measurement system

TLY was measured using a NIM circuit composed of a CANBERRA model 2005 pre-Amp which was connected to the dynode port of the PMT. The pre-Amp output is connected to the Amplifier (Tennelec model TC243) and from there to the Multi-Channel -Analyzer (MCA) that registers the number of counts per channel graph, set to 1 keV/channel by means of the amplifier gain. This way, the circuit integrates over the entire light output of an event, including the fast and the slow component of the scintillation light, and produces an energy spectrum that extends up to the Compton edge of the 662 keV ^{137}Cs line, which is at 473 keV.

Information on the FSCR was obtained using the anode port of the PMT, connected directly to an oscilloscope (Tektronix 2467, 350 MHz). The signal reaching the oscilloscope is not integrated and it primarily reflects the fast scintillation component. The FSCR is obtained by taking the ratio of the peak anode voltage signal to the total energy derived from the TLY measurement. It should be stressed that this is a relative quantity and has significance only when comparing scintillator samples. Thus its values are quoted in arbitrary units.

During the test some instability in system performance was detected. Thus, investigation were conducted to asses the source and magnitude of this instability, as described in appendix C. The result gives ±5% error on TLY when using the calibration method previously described. In order to minimize the uncertainty of results a normalization procedure was implemented. The TLY of calibration sample is measured before and after each sample of interest and then used for normalization. The calibration sample is NE213 (common scintillator) home made cocktail that was sealed in a glass vial in order to prevent its deterioration (see appendix C).

The normalization procedure is as follows:

$$\text{TLY} = \frac{2 \text{ x Channel No. of Sample at the Compton edge}}{\begin{matrix}\text{Channel No. of calibration} \\ \text{Sample Before}\end{matrix} + \begin{matrix}\text{Channel No. of calibration} \\ \text{Sample After}\end{matrix}}.$$

This normalization takes into account the system behavior at the time of measurement, thus minimizing the effect of the instability on TLY values. All light yield measurements (TLY and FSCR) are therefore relative to a single, common standard, namely NE213.

On several of the samples, more rigorous measurements of scintillator light decay as function of time were performed by Ronald Lauck from PTB (see appendix B).

2.4.1 Errors

The most important factor in quantification of scintillator measurement errors is the accuracy of phosphor concentration. It is a combination of errors on weights of phosphors and liquids, errors due to mechanical loses of material when transferring from one vessel to another, weight loss during gas bubbling.

The concentration is calculated as phosphor weight (in mg) divided by solvent volume (in ml). Let c be the concentration, a – the phosphor weight and b – the solvent volume. The relative error on the concentration is then given by:

$$\left(\frac{\Delta c}{c}\right)^2 = \left(\frac{\Delta a}{a}\right)^2 + \left(\frac{\Delta b}{b}\right)^2$$

The most important weight factor is the error in the primary weighing process, determined by the scales which have 0.5mg accuracy. This error is significant only when weighing phosphors since they are measured in milligrams. Other factors give ~0.001% error and are negligible compared to this factor.

In the first stages, sections 2.5.1 – 2.5.2, when all types of solvents and phosphors were tested with 5g/l concentration, the error contribution from weight factors is 2%.

In the later stages, section 2.5.3, when measuring the concentration curves, 5 mg of phosphor were added at each step of the curve. This results in 10% accuracy at each step. In each step the errors propagate, but they may compensate for errors in earlier steps. Assuming a maximal deviation from the measured weight at each step over 12 steps; 6 mg deviation from the 60 mg of total phosphor weight adds up to a total error of ~10%, but due to the compensation, the true value is nearer 7%.

Another measurement error that might contribute is temperature dependence of either scintillator or system. It has been established that scintillator light yield is virtually independent of temperature 23,24), which we confirmed for our final scintillator composition.

TLY measurements have an error due to accuracy in determining peak location ~ 1%. FSCR measurements have errors due to oscilloscope screen accuracy – 8% both on peak anode voltage measurement and on normalized FSCR value. In both cases the error is systematic.

Other possible contributions to errors are: Teflon reflector degraded by optical coupling grease during measurements and errors due to unequal gas bubbling time. All these factors have been carefully controlled during measurement.

Propagating these errors in a manner that takes into account their mutual dependence is a complicated task. Instead, consider the graph in Fig. 12(1), showing the TLY in a part of the concentration curve (section 2.5.3.1) where the TLY is scattered around a steady value. The deviation from the mean value is the total error caused by all the factors mentioned hereby.

The largest deviation from the mean value, which is also the error for all TLY measurements, is 6%.

An analogous procedure for the FSCR in the same concentration curve is presented in Fig. 12(2), yielding a 12% error. This time the steady value sets in at a higher concentration, because the FSCR rise persists at higher concentrations.

The total error accrued by this method for FSCR (12%) is twice the error for TLY (6%). This is plausible considering that FSCR measurements have a typical 8% error in determining the anode peak voltage, whereas the TLY measurements have corresponding errors of only 1% in determining the peak location.

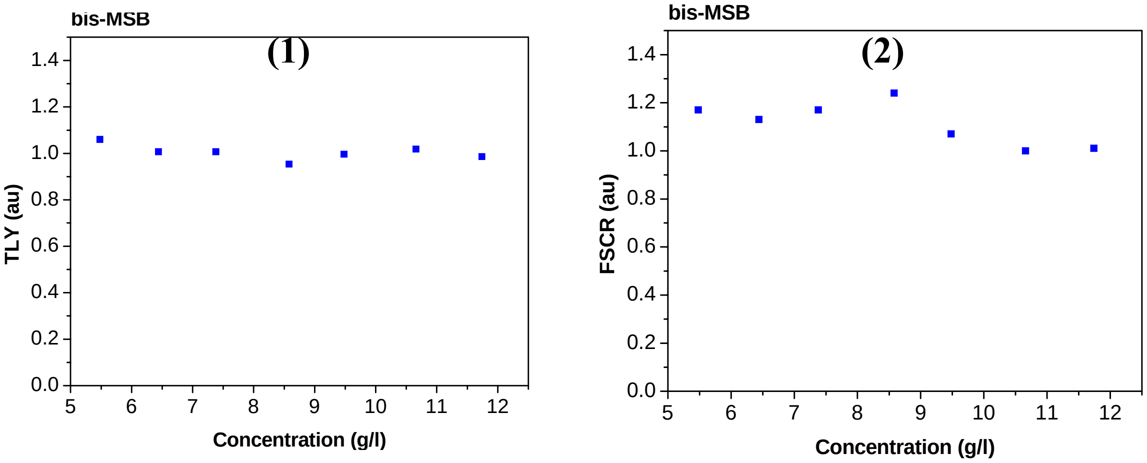

Figure 12: points measured around a fixed value in order to estimate the total error on measurements for: (1) TLY (2) FSCR

2.5 Tests and results

2.5.1 Solvents

First, the relative merits of the solvents were studied using conventional phosphors: PPO and bis-MSB, at typical concentration of: 5-10 g/l. Pure 1MN is liquid, whereas 2MN is solid: their respective refractive indices are n=1.617 and 1.604. However, 2MN can be dissolved in 1MN in virtually unlimited proportions, up to 82% of the total solution.

Table IV: results of solvent tests with [5g/l] of bis-MSB (accuracy of measurements is discussed in section 2.4.1).

Solvent	TLY, normalized*	FSCR, normalized*	comments
1MN	1.08	1.04	
1PN	0.42	0.56	Not all the solute dissolved
65% 2MN +35% 1MN	0.95	1.08	

The 1PN (n=1.66) is a liquid, but it was rejected very early on for two reasons. First, the solubility of the phosphors in it is far too low for scintillation purposes. Second, its light yield is very low, as seen in the results presented in Table IV.

The light output of cocktails based on 1MN / 2MN mixtures with majority 2MN was found to be significantly lower than their inverse-proportion counterparts (with majority 1MN). It is not known whether this is due to inherently more efficient energy-transfer in 1MN, or merely reflects the higher material purity, since manufacturer-quoted assays were considerably better for 1MN (>97%) than for 2MN (>95%).

Thus, 1MN is the chosen solvent for the capillary array detector. As the dominant component, it largely determines the refractive index of the entire cocktail.

2.5.2 Phosphors

In the first round of tests, the light yield and anode peak current of all phosphors listed below in Table V were compared. They were used at a concentration of 5 g/l in 1MN solvent. This concentration is high enough for the cocktail to produce its maximal TLY.

Table V: results of primary phosphors tests (accuracy of measurements is discussed in section 2.4.1).

Phosphor	**TLY, normalized***	**FSCR, normalized***	**comments**
DMPOPOP	0.98	1	Yellow color
TBP (National diagnostics)	0.1	0.17	
TBP (Fluka)	0.08	0.16	
TBP (Aldrich)	0.09	0.16	
bis-MSB	1.01	1.04	Very soluble
α-NPO	0.65	0.67	
PPD	0.05	0.05	
POPOP	0.84	0.9	yellow color
p-Quaterphenyl	0.21	0.09	Very slow pulses
OG - 408	1.2	1.04	
OG - 426	1.12	0.87	

The cocktail containing DMPOPOP gave rather good light yield on the small sample but was eliminated due to its yellow color which could attenuate the light over larger dimensions.

Thus, from this first round two leading candidates emerged: OG408 and bis-MSB, which both yielded high TLY as well as high FSCR. For these two candidates, more extensive tests were conducted, described in section 2.5.3.

Before focusing the investigation on these two candidates, additional scintillator cocktails were measured, in the hope that certain combinations which looked promising on paper will follow through. These combinations include a cocktail of TBP+ PPO, α-NPO + PPO, α-NPO + PPO + bis-MSB. The latter appears to be very fast and may be interesting for other applications. Otherwise, these scintillators turned out to have rather disappointing light outputs.

2.5.3 Concentration curves

The two principal candidate phosphors for the high-refractive-index, special-purpose scintillator are bis-MSB and OG408. At first glance bis-MSB has the advantage of low cost and high availability, whereas OG408 has a light output which is slightly higher. In order to choose between them a more methodical study had to be conducted.

The behavior of these two candidates at different concentrations is the most important factor to study. Concentration of phosphor is very closely related to the light output. The light output usually rises with phosphor concentration until a point, beyond which phosphor addition will not increase the light output. At much larger concentrations phosphor addition may even decrease light output due to quenching effects.

2.5.3.1 Pure phosphors

Each concentration curve comprises a series of measurements at increasing concentrations of candidate phosphor. The base solution is 5 g (~5 ml) of 1MN inside a glass vial. At each step ~5 mg of phosphor were added to the sample, providing a 1 g/l to concentration.

At each step the vial was opened and the pre-weighted 5 mg of phosphor were added. Then, the solution was gently heated in order to accelerate the dissolution process. Once all the phosphor dissolved, nitrogen gas was bubbled through the sample for two minutes, and then the vial was immediately sealed. After winding the Teflon tape reflector around the vial, the latter was attached to the experimental setup as described in section 2.4. At each step both the TLY and FSCR of the sample were measured.

The phosphor concentrations were steadily increased until the light yield saturated: usually several points beyond this point were also measured.

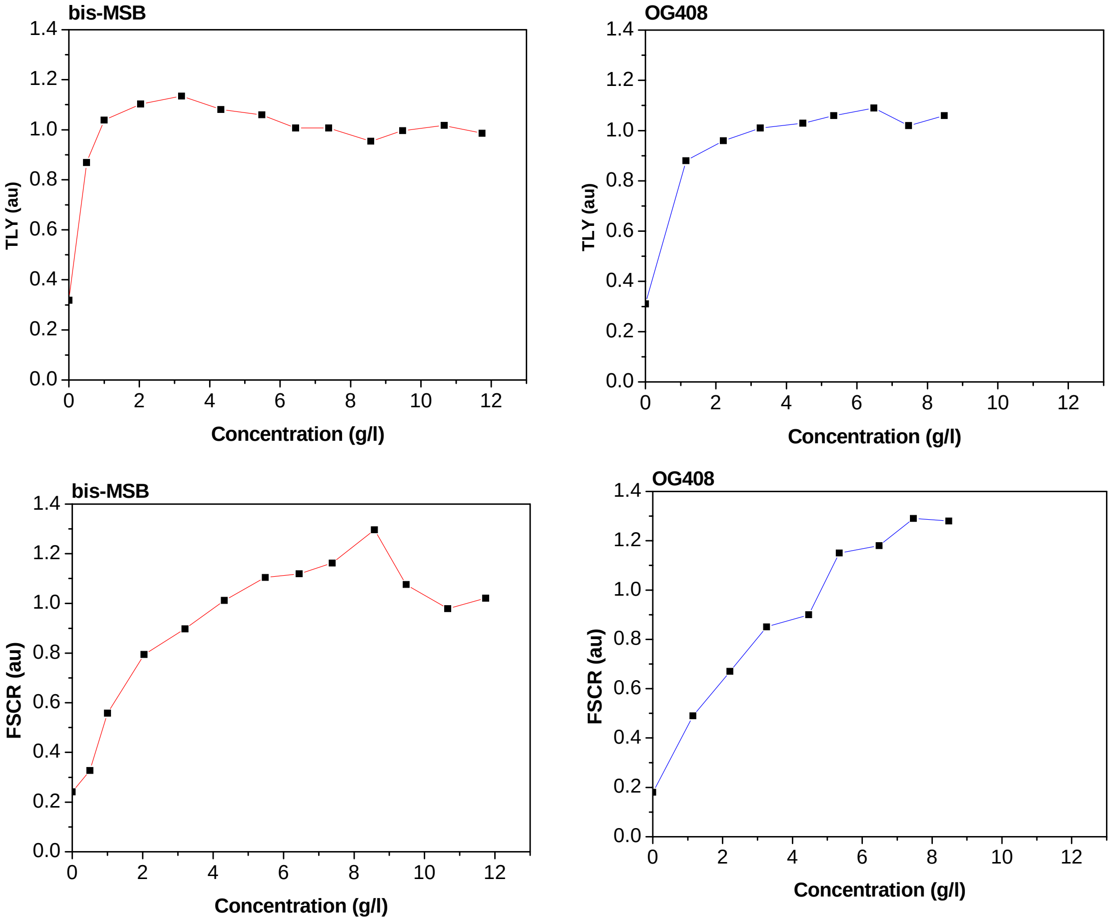

Figure 13: concentration curves of bis-MSB and OG408 in 1MN (upper row: TLY; lower row: FSCR)

The graphs presented in Fig. 13 are the concentration curves for pure bis-MSB and OG408. The saturation point is very distinct in the TLY curves, but in the FSCR curves it is less so. The probable reason is that the FSCR measurement error is twice as large as its TLY counterpart - 12% comparing to 6%.

The maximal TLY in these curves is similar for bis-MSB and OG408. In the preliminary measurements for 5 g/l concentration, the light yield of OG408 was significantly (20%) higher. In Table VI and Fig. 14 some old values of OG 408 are compared to the new values. The old values are consistently higher than the new.

The difference in these values is explained by the change in the calibration scintillator sample. The scintillator itself is unchanged, but the reflector was changed in the month between the old set of measurements and the measurement of the OG408 concentration curve. The new reflector increased the total light output of the calibration sample, thus diminishing the normalized TLY of the OG408 cocktail samples.

From the shape of the new concentration curve it is clear that at concentration of 5 g/l OG408 is already at its maximum TLY value – 1.2 in the old measurement. For bis-MSB, the maximum TLY value of 1.13 is attained at 3.2 g/. The conclusion is that OG408 has marginally better TLY than bis-MSB, by ~6%, but the maximal TLY is reached at different concentrations for each phosphor.

Moreover, it can be deduced from the shape of these TLY concentration curves that the saturation point of bis-MSB is reached at lower concentration. The quenching of bis-MSB also sets in at lower concentration than in OG408, which does not seem to reach saturation at all.

Table VI + Figure 14: comperison of old TLY values for OG408 to new TLY values (accuracy of measurements is discussed in section 2.4.1).

Conc. (g/l)	Old TLY	New TLY
0.75	0.83	0.69
2.5	1.11	0.97
5	1.2	1.04

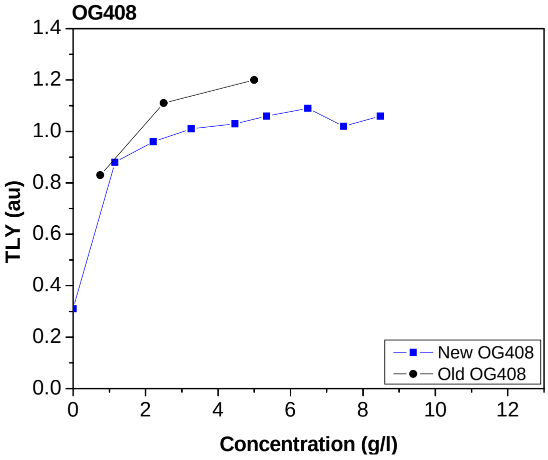

It is also clear from these curves that the FSCR ratio of OG408 is higher than bis-MSB. This does not directly affect the GRA application, but may have importance in future applications.

2.5.3.2 Phosphors with PPO

Commonly, PPO is added to scintillators to increase their light output. Concentration curves with fixed bis-MSB concentration and varying PPO concentration were measured. It was important to check the PPO effect on the light yield since, in the GRA application, the light output is crucial.

The base scintillator sample for this measurement set is 5 g of 1MN + 2.5 g/l bis-MSB.. PPO is added in ~10 mg = 2g/l steps. Again, the steps were continued until the concentration was well passed the saturation point – see Fig.15.

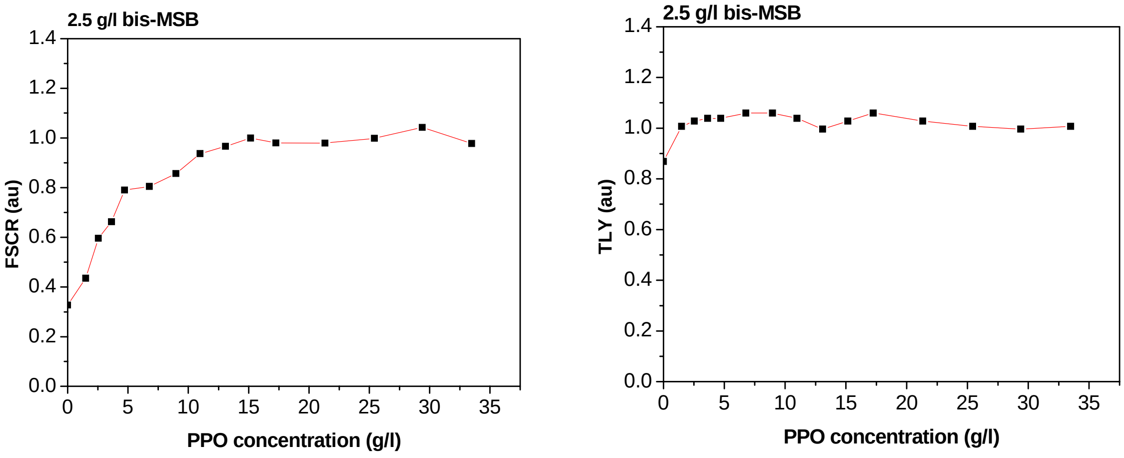

Figure 15: concentration curves of PPO added to 1MN + 2.5 g/l bis-MSB

(1) FSCR vs. PPO concentration; (2) TLY vs. PPO concentration

Comparing to the concentration curve with pure bis-MSB it is evident that the maximum TLY is the same for pure bis-MSB and for bis-MSB + PPO. With the application in mind, it is clear that PPO does not help to improve the light yield above the maximum value reached with pure bis-MSB.

In theoretical terms, this upper limit on the TLY implies that the exact mechanism in which the energy is transferred from the solvent to the bis-MSB molecules (directly or through PPO molecules) is unimportant to the maximal TLY reached.

In order to assume similar behavior for OG408, Fig. 16 presents the data points measured for OG408 with and without PPO addition in the first round (old measurements):

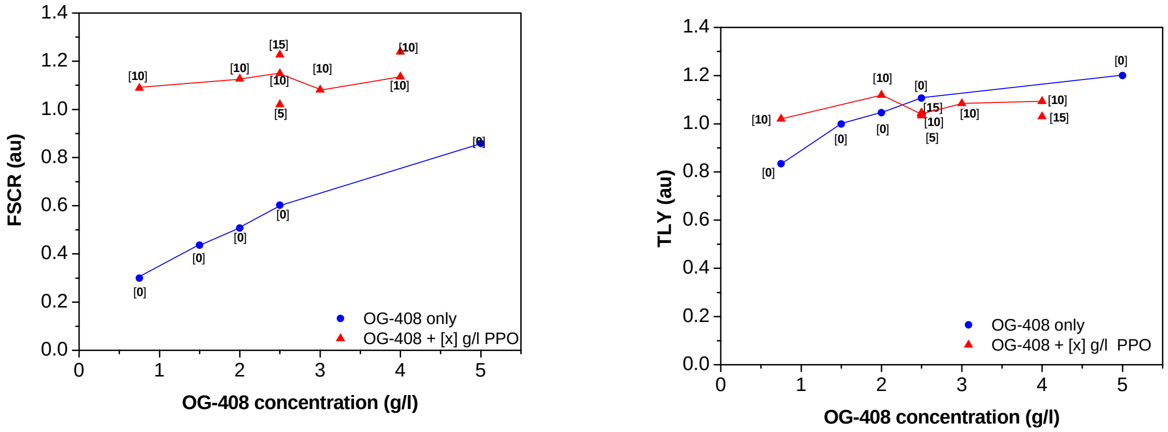

Figure 16: OG408 with and without PPO addition. (1) FSCR; (2) TLY

For concentrations below the saturation point, the PPO increases the TLY, whereas for concentrations above, PPO addition actually reduces the TLY.

Assuming such upper limit on the TLY of OG408 + 1MN leads to the conclusion that OG408 causes less quenching than bis-MSB. The reasoning is as follows: The charged particle incident on the scintillator transfers energy to the solvent molecules. In a binary solution, this energy is transferred directly to the phosphor. In a ternary solution, this energy is transferred to the secondary phosphor both directly and indirectly, through the primary phosphor. A part of the energy invested in the secondary phosphor may be lost to quenching.

Both cocktails containing 1MN as a solvent exhibits an upper limit on TLY. This suggests that limited energy can be invested in excitation of the 1MN molecular energy levels that contribute to the scintillation process. Comparing the cocktails containing only a single phosphor, the OG408 cocktail has a higher TLY than the cocktail containing bis-MSB. This suggests that less energy is lost by quenching.

The FSCR graph indicates another interesting fact: PPO helps to increase the FSCR of scintillator composed of 1MN + OG408. Again, this may prove significant in future applications with capillary array detectors.

2.6 Final cocktail

Based on all the data acquired the final composition of the special-purpose scintillator could be decided. The first usage of this scintillator was in the preliminary Bern experiment in November 2006.

If the maximal light yield of scintillator with the two candidate phosphors is equal, either can be used. For the Bern experiment we chose to use bis-MSB because OG408 is less readily available. We chose to add to the cocktail some PPO which made it a faster scintillator, changing the FSCR values from 0.93 to 1.07 without changing the overall light output.

The cocktail used for the Bern experiment:

1MN + 3 g/l bis-MSB + 5g/l PPO

2.7 Resonant-response detector

The capillary array detector in the GRA context should serve as a resonant-response detector. For this purpose a nitrogen-rich-additive should be added to the cocktail mentioned in the previous section. This proprietary additive will be named here NRA. It was found during the development of the scintillator for the bulk detectors.

The NRA was selected since, in addition to its high nitrogenous content, it is least detrimental to the scintillation process. Doping a scintillator with NRA causes a decrease in the light output that is linear with the scintillator concentration in the new solute, i.e., a scintillator diluted with 25% NRA will have 25% less light output. This is the best possible case, in which the NRA behaves as a passive bystander in the scintillation process. Under less favorable conditions, the NRA will quench the scintillation light: the yield will then deteriorate, much faster and at relatively low dopant concentrations.

This NRA does not change the time dependence of the scintillator light as seen in appendix B, thus supporting the claim that it does not actively detract from the light yield.

Large amounts of NRA need to be added in order for the resonant process in the detector to be adequately efficient.

After the Bern experiment a second cocktail was used to refill the capillary array detector. This time, a nitrogenous scintillator was used in order to create a prototype of the final resonant capillary array detector. The nitrogenous scintillator is composed of a special-purpose newly-developed scintillator with addition of NRA. This time, the cocktail containing OG408 was used.

The cocktail used for the nitrogenous scintillator:

1MN + 5 g/l OG408 +10 g/l PPO +7.3% NRA ; total nitrogen: in the percent range

3. Bern experiment

3.1. Preamble

In order to perform the preliminary proof-of-principle experiment the capillary array had to be built, filled and sealed in its custom designed housing. Also, the data readout system had to be made to the appropriate specifications. All these tasks were performed by I. Kreslo from the Laboratory for High-Energy Physics, University of Bern, on the basis of his experience, using equipment deriving from the CHORUS experiment [9,12-14)].

Soreq's role, apart from proposing the application and initiating the collaboration, concentrated on optimization of the high-refractive-index-scintillator, performing Geant4 simulations and participating in the first Bern test.

The principal goal was to reactivate the CHORUS detector and test it with gamma-ray and mixed gamma-neutron events produced by radioactive sources.

3.2. Cell /array configuration

3.2.1. Capillaries

The array was composed of ~20 µm diameter capillaries with spacing ~11 µm wide, manufactured by Schott Fiber-Optics. The capillaries are arranged in hexagonally shaped aggregates, also named "multies". These multies are then brought together in a beehive structure to create larger arrays of millimetric size.

The matrix is made of Schott Technical Glass Type 8250, and incorporates extra mural absorbers made to absorb light in order to improve localization of detection. The matrix glass has low refractive index to enhance the total internal reflection effect (section 1.2.3, 1.2.4), and the inner surface is smooth in order to reduce losses due to imperfect total light reflection.

Fig. 17(a) shows a single capillary with sizes determined using the SEM system. The measured diameter of the capillary is 19.46 µm, which is reasonably close to the quoted 20 µm. The average wall thickness is 11.37 µm with small deviations. The photo also shows the voids between neighboring capillaries, evidence to the fact that these were manufactured separately and subsequently brought together. From Fig. 17(b) and 17(c) the lateral extension of the multies can be deduced as ~400 µm wide.

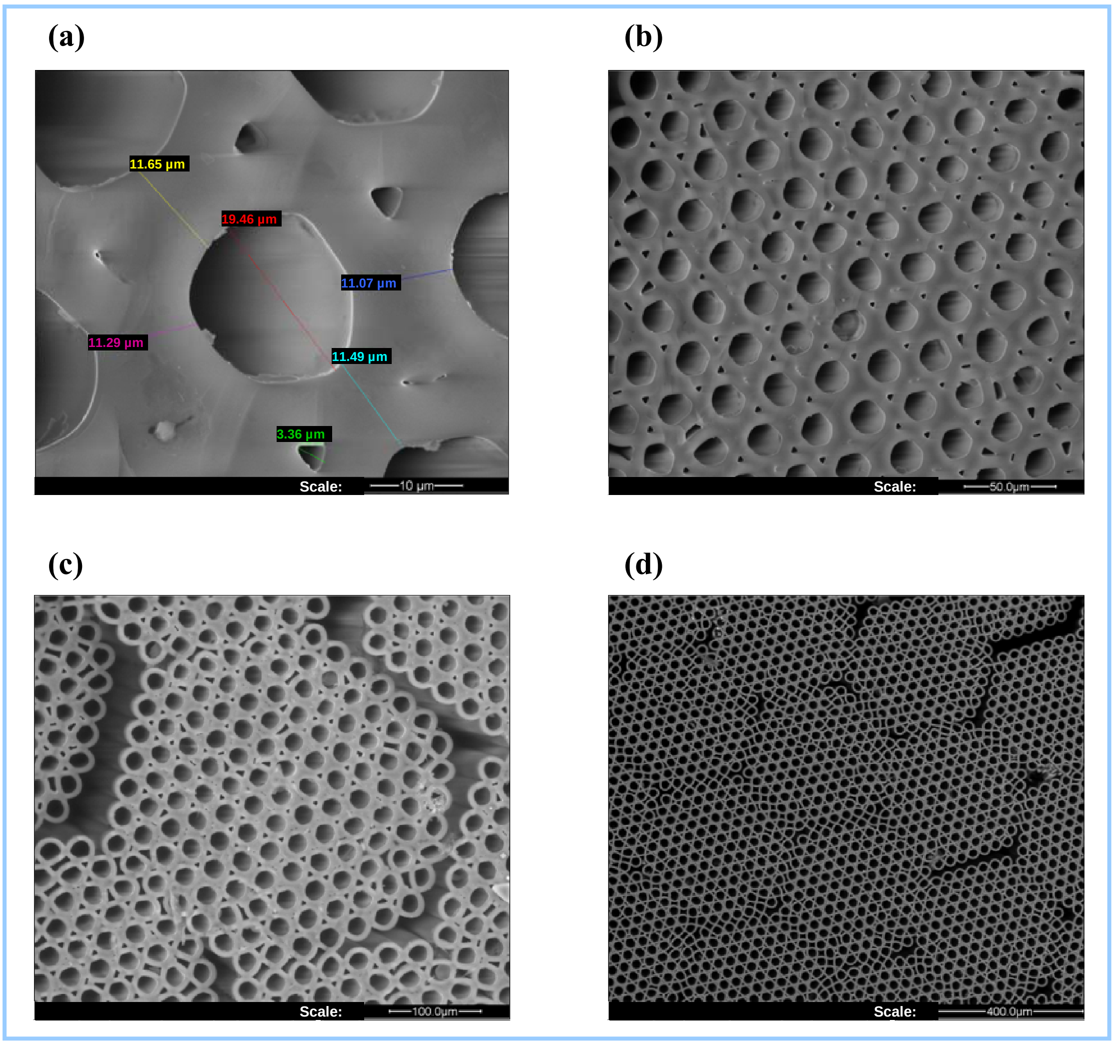

Figure 17: SEM pictures of capillary array of the same type used in the Bern experiment, subsequently taken at Soreq NRC. With increasing frame No., the scale zooms out: (a) 10 µm (b) 50 µm (c) 100 µm (d) 400 µm.

The manufacturing process for capillaries of similar type for an elementary-particle physics application is documented 9). It commenced with an 8250-glass tube of 43 mm outer diameter being drawn to a diameter of 1.84 mm. These mono-capillaries were stacked to form a hexagonal array of 547 units and were placed inside a tube of 8250 glass. Black glass rods were inserted in the interstices between the mono-capillaries to act as EMA. The assembly was then drawn to give a hexagonal "multi" measuring 1.7 mm between opposite flat sides. Finally, 940 multies were gathered in a close-packed pattern, and were inserted into a square glass tube, constituting the outer part of the bundle. This assembly was drawn to the desired final dimensions.

Capillaries were manufactured in lengths of ~1 meter. This length was required by the CHORUS experiment but it is redundant for the GRA application. Therefore, the array was cut to ~11 cm length.

The hexagonal array presented in Fig. 18(a), was used to construct a larger array, composed of 7 such subarrays (see Fig. 21), the filling of which failed. The square array presented in Fig. 18(b), was then used for the rest of the experiment.

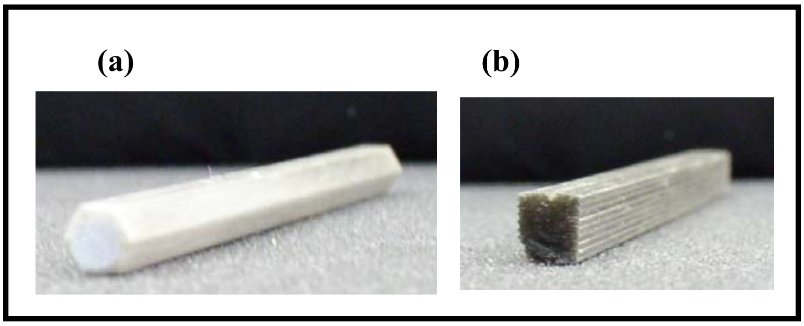

Figure 18: Two types of capillary arrays used in the Bern experiment. (1) Hexagonal array (2) Square array. The black/white color of the array faces is the result of cut quality.

The total size of each square array is 5 x 5 mm^2. Four such arrays were glued together to form the larger 10 x 10 mm^2 array used in the experiment. The larger capillary array (10 x 10 mm^2) was then placed inside an aluminum tube, and the gap between them filled with silicon RTV elastosil E41, chosen for its durability when exposed to the liquid scintillator.

Cutting the array to its final size of 11 cm, so that its tips will not protrude out of the tube was carried out using a fine grain diamond saw rotating at 7000 rpm under a flux of cooling liquid. During the cutting process, air was forced through the array so that the splinters created would be blown away and not penetrate the capillaries, or stay on the surface. The assembled tube was then placed in its cell.

This process could be improved by ensuring that the motion of the saw is totally perpendicular to the array, so that its face obtained is smooth and level.

3.2.2. Detector cell description

The detector includes the capillary array housing, including the necessary equipment to attach the cell to the liquid filling system and optical readout. The detector is displayed in Fig. 19 alongside its schematic diagram.

The array is pressed against a Fiber Optic Plate (FOP) on one side and a glass window on the other, using aluminum flanges. The contact between the flanges and the tube is sealed using silicon gaskets

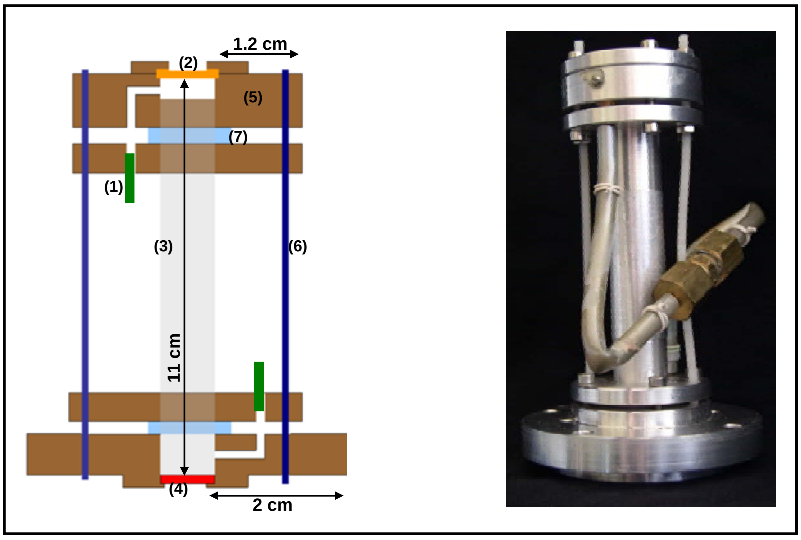

Figure 19: detector scheme and photo. In the scheme: (1) liquid inlet/outlet, copper feed-through plastic tubes; (2) glass window; (3) tube filled with array and silicon RTV; (4) FOP; (5) aluminum flanges; (6) plastic rods; (7) silicon gasket

To achieve highly-localized light-transport and optimal spatial track imaging, the face of the capillaries should ideally be in contact with the FOP over its entire surface. However, since the capillary cutting process was flawed, good coupling could not be achieved. Tightening the flanges needs to be done carefully in order not to break the capillary array face or the FOP, particularly if the array face is not absolutely planar and parallel to the FOP. Plastic rods parallel to the tube are used to ease the pressure on the capillaries face.

The connection to the filling system is via a copper feed-through and the plastic tubes seen in Fig. 19 that are first connected to the filling system and then to each other, creating a stand-alone detector cell.

3.2.3. Filling procedure

After the detector is assembled, the capillaries are filled with the special-purpose liquid scintillator. The filling procedure [9)] is not trivial because of the naturally-occurring countering forces, such as the liquid surface tension and viscosity. A special filling system was designed to overcome these forces, based on the one used in the CHORUS experiment.

The filling system (Fig. 20) functions by repeatedly flushing the array with the liquid scintillator, which is shunted back and forth between the two blue reservoirs, using low-vacuum suction. It takes several hours until all capillaries are filled.

To maintain scintillation light output, the system is first flushed with argon gas that eliminates the oxygen in the system. The scintillator in the reservoirs is also bubbled with Argon gas to reduce dissolved molecular oxygen.

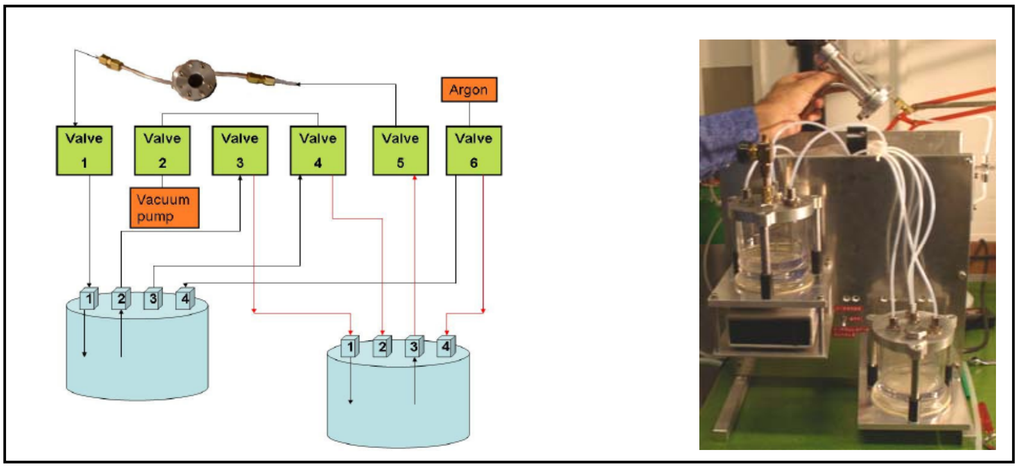

Figure 20: schematic diagram and photo of filling system

The principle of total internal reflection can be used to determine whether the filling process was successful. When the capillaries are empty the refractive index of the air inside them is lower then the cladding refractive index. Thus, none of the light will be internally reflected and the array face will appear black.

If the capillaries are filled with high refractive index scintillator, some of the light undergoes total internal reflection and the array face will appear bright. Therefore, looking at a light source through the glass window of the capillary array detector reveals whether the filling process was successfully completed.

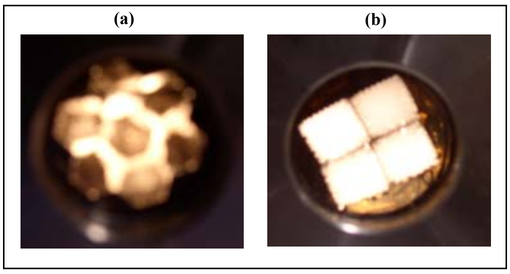

Figure 21: comparison of capillary arrays filled with scintillator. (a) poorly-filled array; (b) an array filled successfully

An example of this behavior is presented in Fig. 21. In section 3.2.2 two large arrays are mentioned. The first of which, composed of the hexagonal array was built, but was not successfully filled. In Fig. 21(a) it is seen after a partially successful filling. A light bulb was placed behind the FOP and the photo is taken looking at the glass window on the other side of the array. Fig. 21(b) is the photo of the square array configuration successfully filled.

Although this crude method cannot detect individual empty capillaries it gives a good indication of a filling process that was adequate for the requirements of this preliminary experiment.

3.2.4. Readout

The Readout was refurbished from the old CHORUS system 9) with one major change: the capillary array used in the Bern experiment is only ~11 cm long, compared to 3 m originally used in this system. Fig. 22 is a schematic diagram of the readout system.

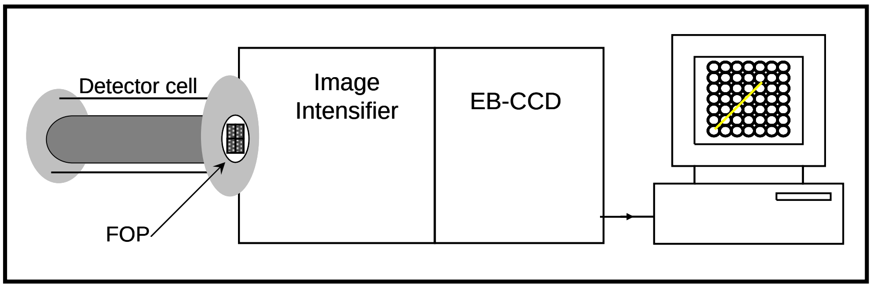

Figure 22: diagram of the readout system.

The first stage of the refurbished optical imaging system comprises an Image-Intensifier (I-I) that is attach to the exit window of the array FOP, 1024 x 1024 pixels, each 13 x13 μm^2. The unit cell size of the capillary array is only ~25 μm^2 (capillary diameter + cladding) so there is no loss of resolution due to the FOP. The first I-I has an electrostatic photocathode at the entrance and phosphor output.

The next stage is an electron-bombarded-CCD (EBCCD) with an electrode gating, which combines the functions of an electrostatically-focused I-I and a conventional CCD. It is essentially an I-I with the phosphor screen replaced by a back-thinned CCD. The EBCCD output is displayed on a computer screen using a ROOT software interface. Both the I-I and the EBCCD were produced by Geosphera 9). The magnification is m = 0.625 for the first I-I and m = 0.83 for the EBCCD. It was originally designed to be used with green-emitting scintillator, so our blue-emitting scintillator decreased its efficiency by ~20%.

The FOP was not in good physical contact with the back end of the array, allowing some liquid scintillator to migrate into the gap. Light created in a single capillary expands as it traverses this scintillator, causing a "blooming" effect". This has the effect of delocalizing the pixel information and thus tends to blur the track images.

During the experiment a principal deficiency of this readout was encountered. The residual gas inside the camera gives rise to large ion pulses, which are clearly visible on the screen.

3.3. Signal shape

In this experiment the light output from the entire array was measured and compared to that of a plastic scintillator. The goal of this experiment was to compare the capillary array signal to a bulk scintillator signal. The Compton-edge pulse-height and shape were compared as well as the experimental and calculated yields of photo-electrons emitted inside the capillaries.

The setup of this experiment consisted of bulk green plastic scintillator with reflective Teflon coating, coupled to photomultiplier (PM-B1-56AVP-No.28) using optical grease (Bicorn BC630). The PMT signal is visualized on the oscilloscope (Tektronix 016-0082-00). This setup collects most of the light produced inside the plastic scintillator. Naturally, when the array was tested the array cell replaces the bulk plastic scintillator in this setup, with one side of the detector cell attached to the PMT using the same optical grease. Since only ~9% of the light arrives at each capillary end, only this fraction of the scintillation light produced inside the capillaries was collected.

The first test of the capillary array behavior involves comparing the signals from the bulk plastic scintillator (using ^{137}Cs source) to the signals from the capillary array in the setup described above. The results are presented in Fig. 23.

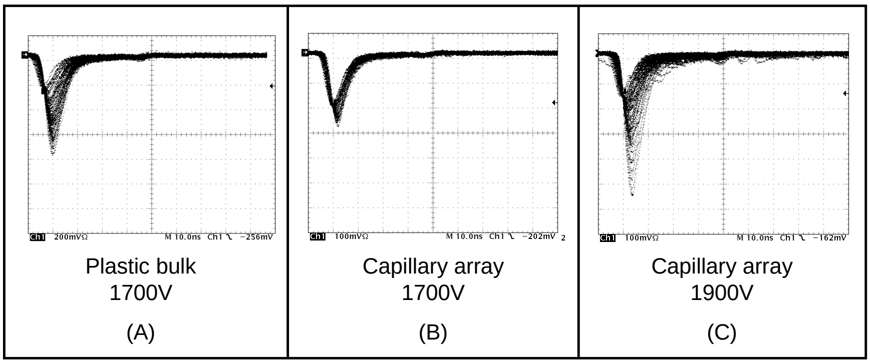

Plastic bulk
1700V
(A)

Capillary array
1700V
(B)

Capillary array
1900V
(C)

Figure 23: signal as recorded on the oscilloscope. (A) Bulk plastic scintillator; (B) Capillary array, same voltage on PMT as in (A); (C) Capillary array, higher voltage on PMT

Fig 23(A) shows the signals received from the bulk plastic scintillator with 1700V on the PMT tube and low threshold which allows the entire ^{137}Cs source spectrum to be displayed. The highest signals are the Compton edge of the spectrum – using relativistic kinematics the Compton edge of the ^{137}Cs 662 keV line is at 473 keV.

The signals from the capillary array are displayed in Fig. 23(B) and 23(C). Fig. 23(B) is for 1700V, the same voltage as in Fig 23(A). But the signal had to be amplified, so the voltage was raised to 1900V and the discriminator lowered accordingly, yielding Fig. 23(C). The first promising sign in these spectra is that the capillary array signal is essentially identical to the bulk scintillator signal. They have the same pulse shape and amplitude distribution.

The differences between the signals are clear and can be explained easily. First, the 1700V bulk-scintillator signal is flat over most of the pulse-height range and exhibits a small peak at the Compton-edge, whereas the capillary spectrum exhibits less and less events with increasing pulse-height. The reason is that for ~23 μm diameter capillaries the high energy electrons (maximal energy 473 keV at the Compton edge) tend to escape the array and deposit only a fraction of their energy in scintillations

The maximum pulse height is 300 mV for the capillaries, and 820 mV for the bulk plastic scintillator – a factor of 2.73. Since the PMT on the array detector side collects only 9% of the light produced inside the capillaries, the difference was expected to be much larger. Possible explanations are:

- There is scintillator inside the detector enclosure but outside the capillaries. Most of it is located at the capillaries end, between the silicone and the FOP. For all purposes, it behaves as bulk liquid scintillator
- Plastic scintillators yield ~83% of the light that our liquid scintillator yields.

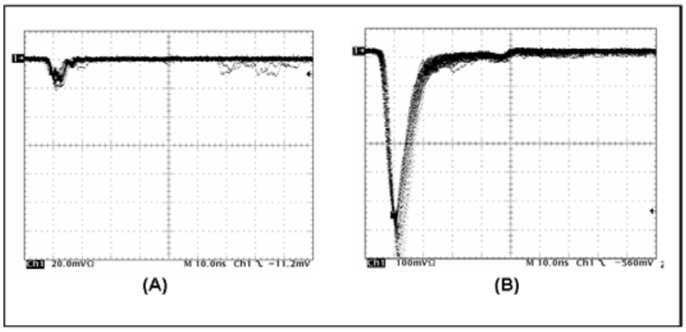

Figure 24: signal on oscilloscope, 1900V on PMT, capillary array detector (A) single electron events (B) Compton peak of ^{137}Cs

A second test for the validity of the capillary array as scintillator is calculation of the photoelectrons created by a Compton peak electron in the scintillator.

Fig. 24 presents data taken at 1900V PMT voltage: Fig 24(A) shows single electron events with average amplitude of 10 mV. This permits to determine the number of photo-electrons produced by ^{137}Cs source γ-rays. In Fig. 24(B) the Compton-edge of these γ-rays is seen. Their pulse height is ~700mV, which corresponds to about 70 photoelectrons per event at the photocathode. Since the latter has 20% quantum efficiency, this implies that 350 scintillation photons are incident on the photocathode at this energy. These correspond to the 8% fraction of the scintillation yield integrated, so that, in total, for such 473 keV event maximal deposited energy corresponds to 4375 photoelectrons. In regular organic liquid scintillator, 1 MeV electron yields ~10,000 photoelectrons; So 470 keV electrons should yield ~4700 photoelectrons. The deviation from the expected value is only 7.4%, which constitutes excellent agreement considering the crudeness of the approximation.

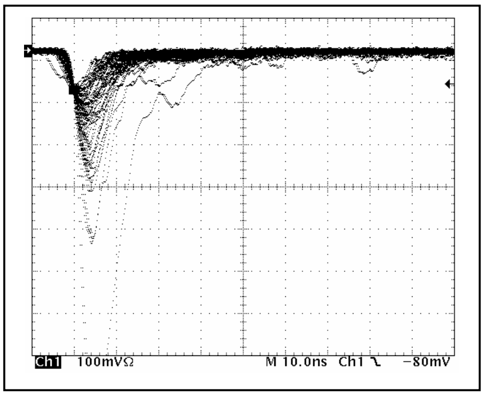

Figure 25: ^{239}PuBe mixed source, capillary array detector signal.

The final Fig. 25 displays the signals generated by the ^{239}PuBe mixed gamma and neutron source (of intensity 2.5 x 10^6 neutrons/s) used in the second part of the experiment, on the new detector cell. The highest pulses are > 600 mV, corresponding to more than ~450 keV electron energy, but the rate of high amplitudes is only few pulses/sec – this affirms the observation of very low proton-track count rate with the image intensifier (one in ~5-10 s).

These results are not conclusive; the capillary array signal shape is deceivingly promising at first glance. But serious flaws remain – the question whether this signal is actually produced in the capillaries or is it mere noise from the extra-capillar liquid that may be swamping the true capillary event signals.

3.4. Experiment and results

3.4.1. Cosmic rays

In the first stages of the Bern experiment several long tracks were detected, that were too long to constitute electron events. It is presumed that these were due to cosmic rays which dissipate only small fractions of their energy in the scintillator. In order to substantiate this assertion, the ^{239}PuBe source position was altered several times, so the gammas coming from the source would impinge on the capillary array from different directions, thereby changing the electron tracks. Finally, when the ^{239}PuBe source was returned to its shielded housing, and room background data taken, the long tracks were unaffected, thus demonstrating they were unrelated to the gamma rays coming from the source.

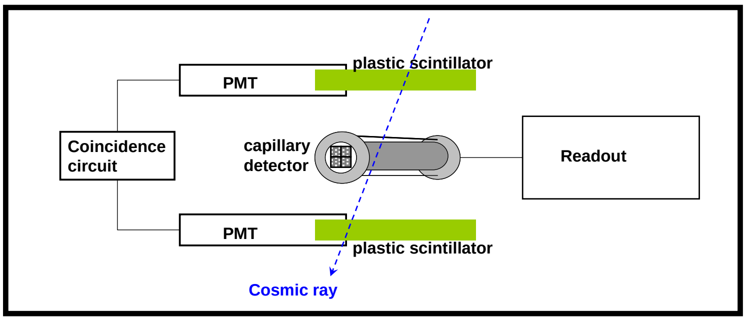

Figure 26: setup of cosmic rays telescope.

The setup presented in Fig. 26 was designed to eliminate such cosmic rays. An ionizing particle incident from above will pass through both plastic scintillators in addition to the capillary detector. Thus, simultaneous pulses in both PMTs will trigger the coincidence circuit. Whenever this occurs, the coincidence circuit (operated here as an anticoincidence event veto), suppresses the trigger of the readout system.

3.4.2. Particle tracks

During the experiment the image on the capillary screen was recorded using the readout system. Its trigger was provided by the anti-coincidence circuit. The photos were taken automatically with pre-set exposure gate times and intervals between exposures. The gates were in the range of 300 µs -100 ms. The lower limit on gate time was determined by the first I-I, the decay time of its phosphor being ~200 µs. The threshold for taking an event image was set so that the maximum numbers of tracks are visible while most of the noise (predominately single-pixel) is eliminated. Eventually, the optimal conditions were found, and ^{239}PuBe source images were recorded with 1 ms gate and 500 mV threshold.

The energy of neutrons emitted from ^{239}PuBe source is predominantly below ~ 5 MeV [25)], giving rise to a maximal track length [26)] of ~400 μm. However, the neutron conversion probability is higher in the 1-3 MeV energy range, leading to a majority of 0.5-1.5 MeV protons. Moreover, since the ~0.5 MeV protons give rise to considerably lower scintillation light due to quenching, a reasonable assumption is that most of the registered events are protons with ~ 0.8-1.5 MeV energy range.

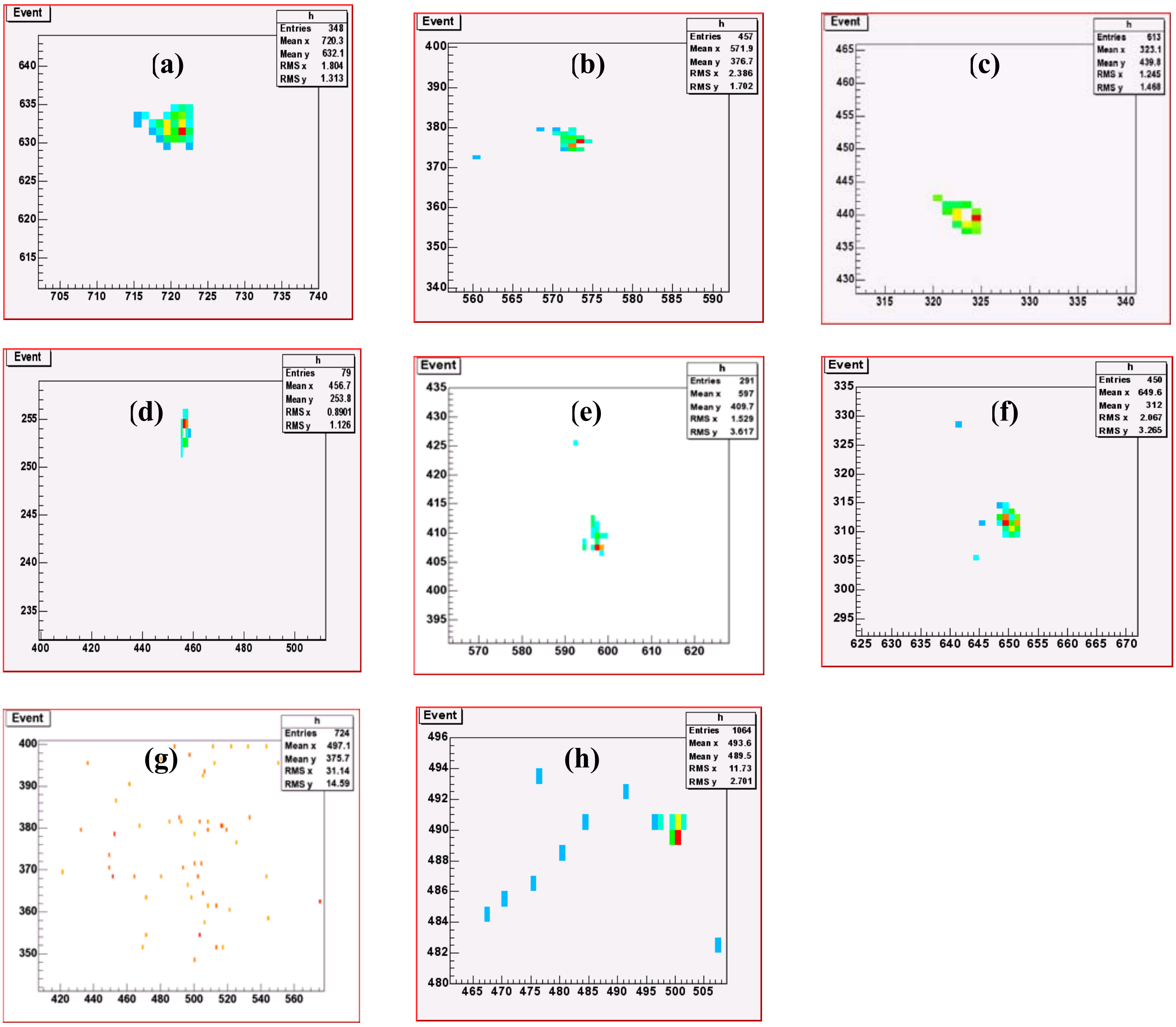

Figure 27: (a),(b),(c),(d),(e),(f) - tracks of recoil-protons produced by neutrons; (g) low energy electrons (h) simultaneous events: high energy Compton electron and a recoil-proton.

As seen in Fig. 27 (a)-(f), recoil-protons produced by neutrons give rise to bright, short tracks. In all the proton events displayed, there are indications of the Bragg peak, which manifests itself as a bright agglomeration of light near the end of the particle range.

Moreover, since individual pixel size is 13 X 13 μm^2 (the I-I resolution), the protons events presented have track length of up to ~65 μm, in agreement with the above estimate.

In these high-light-intensity events a "blooming" effect can be observed (section 3.2.4).

High-E Compton electrons produced by 4.43 MeV γ-rays give rise to faint, long tracks, presented in Figs. 27 (g), (h). Low energy electrons from "soft" Compton interactions in frame 27(g) show up as faint, single-pixel events. Six in-line pixels in frame 27(h), present a more energetic electron track. It is also evident that minimum-ionizing particles do not produce enough light to create an uninterrupted track. This was one of the main drawbacks of detector for the CHORUS application.9)

The electron background is caused by non-resonant γ-rays, as well as resonant gamma rays that did not undergo a resonant reaction. The non-resonant background is independent of the nitrogen content of the inspected object, and should be subtracted to yield the net resonant γ-rays arriving at the detector (see section 1.1.2).

The number of resonant γ-rays that create electrons via non-resonant reactions can be calculated from photo-protons number using the reaction cross-sections. Consequently, whereas proton identification is essential for the GRA application, the principal role of electrons is in the nitrogen-image normalization procedure and counting single tracks is not necessary.

The faint, long tracks of electrons are clearly very different from the strong bursts of light over a short trajectory that characterizes the proton tracks. Thus, even though electron tracks were scarcely visible, clearly the protons could be detected and discriminated from the electron-background. For a first attempt, this experiment yielded very promising, albeit qualitative, results.

4 Monte Carlo simulations

The simulations were performed using Geant4 simulation Toolkit, version 4.8.0, distributed by CERN [17,18].

4.1 Preamble

The simulation is designed to yield quasi-empirical probabilities for electron/positron-producing scintillation events (from non-resonant gamma-ray interactions). These are required to verify that the resonantly-produced photo-proton events are indeed detectable. These simulations are necessary but not sufficient for a proof-of-principle, since the actual processes in the capillaries cover a much wider range of physical phenomena than can be simulated within GEANT4, such as light collection processes in the capillaries themselves or in any other part of the readout system

At 9.17 MeV photon energy, the dominant non-resonant interaction process (see section 1.3.3) is the Compton effect, pair production being weak (as the scintillator is low-Z) and photoelectric contribution essentially negligible. All these interactions are included in the simulation application written here.

Secondary, tertiary (… etc.) electron interactions in this simulation include Ionization (the principal process inside the scintillator), multiple scattering and Bremsstrahlung. Positron processes include annihilation as well.

4.2 Benchmarking

Before beginning the overall system simulations, several basic simulations were performed in order to insure that Geant4 is working properly in the energy range and material densities of interest, since it was originally intended for considerably higher energies.

The benchmark simulation was of a large scintillator bulk inside a quartz cylinder of density 2.23g/cm^3. The first stage involved shooting 662 keV gamma rays at the center of the sample in order to check if this yields the same spectrum as obtained in the lab.

This stage was particularly useful in debugging diverse aspects of the data extraction procedure. Indeed, the Compton peak was observed precisely at the expected pulse height.

Another check of Geant4 was to count the number of gamma events produced in the scintillator. Using theoretical cross-section values [10], this number was calculated for 3000 events of 9.17 MeV gammas incident on the scintillator. The latter has an elemental composition of 85% Carbon + 10% Hydrogen + 5% Nitrogen, and a total density of $0.95 g/cm^3$, simulating nitrogen-rich scintillator composition.

18% of these gammas are expected to interact with the scintillator. Geant4 predicts 18.13%, or a total of 544 events, 442 of which are Comptons and the rest - pair production. The semi-empirical estimate, based on tabulated attenuation coefficients [10)] for 10 MeV photons, predicts a total of 545 events, 444 Comptons and 101 pair-production events, in excellent agreement with Geant4.

4.3 Single capillary simulations

Fig. 28 shows how a single capillary responds to a 9.17 MeV source perpendicular to its principal axis (see plot 28(a)). In each simulation run, $2x10^6$ γ-rays were incident on the capillary and generated electrons. For each interaction event, the simulation tallies the total energy deposited by all primary and Delta-electrons inside the scintillator.

It is evident from Figs. 28(b) and 28(c) that some electrons deposited energies up to ~0.5 MeV in the 1000 μm capillary, but most deposited less than 0.25 MeV. As expected, in the 50 μm capillary (fig. 28(B)), the deposited energies are significantly lower.

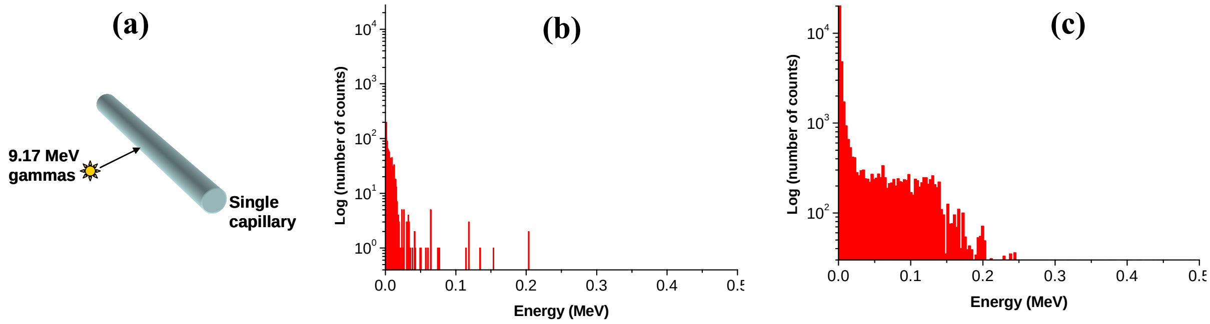

Figure 28: Capillary response to 9.17 MeV γ–rays incident perpendicular to principal axis.

(a) Illustration of simulation geometry

(b) Capillary of diameter 100 μm: Electron spectrum vs. deposited energy.

(c) Capillary of diameter 1000 μm: Electron spectrum vs. deposited energy.

To complete this series of simulations, the response of a capillary to 9.17 MeV γ-rays incident along its principal axis (Fig. 29(a)) was investigated. As before, the code tallies the energy each electron deposits in the scintillator. In contrast, in the present case, forward-going electrons deposit an appreciable fraction of their energy in the capillary itself. Moreover, the larger the capillary diameter, the higher the electron energy deposited. This is clearly shown in plots 29(b) and 29(c), which show the deposited electron energy spectra in capillaries of 50 μm and 3000 μm diameter, respectively.

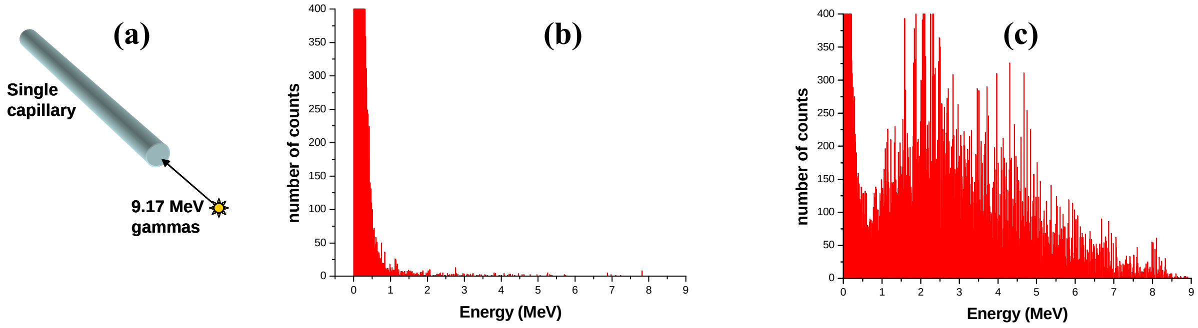

Figure 29: Capillary response to 9.17 MeV γ-rays incident along principal axis.

(a) Illustration of simulation geometry

(b) Capillary diameter 100 μm: Electron spectrum vs. deposited energy.

(c) Capillary diameter 1000 μm: Electron spectrum vs. deposited energy.

These simulations (in both perpendicular and longitudinal geometries) clearly demonstrate that electrons produced in the liquid-scintillator core of the 50 μm capillary deposit little energy there, in contrast to the resonantly-produced 1.5 MeV photo-protons whose range in the scintillator is ~51 μm.

4.4 Capillary array

Three variances of this geometry were used in the simulation. The first capillary array Geometry is illustrated in Fig. 30. In order to simulate an array, equi-distant, cylinder shaped "incisions" were made in a square block of scintillator-like material of appropriate dimensions. How well this approximation represents a realistic capillary array can be demonstrated by comparing to Fig. 17, section 3.2.1 - the array in the Bern experiment

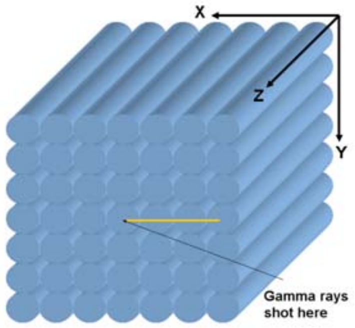

Figure 30: Geometry of simulation (model for geometry 1) parameters are specified in the first row of Table VII.

Smaller capillaries offer superior tracking resolution, but below a certain diameter electrons may deposit insufficient energy in some of the capillaries, thus giving rise to a discontinuous track. The three geometries simulated differ in capillary diameter, distance between neighboring capillaries and number of capillaries in an array. These parameters were varied in order to find the optimal tradeoff between full tracking capabilities and high resolution.

Another parameter checked is the difference in the energy spectra between the first and last capillaries participating in a track (the central capillary and the last capillary). In order to make such comparison the array XY plane (see Fig. 30) needs to be of the same magnitude in all three simulations, thus requiring an array of smaller diameter capillaries to contain more capillaries. The parameters of each array simulated: size, number of capillaries etc. are specified in Table VII.

Table VII: details of different simulations array geometry

Geometry #	Diameter (µm)	Wall width (µm)	Number of capillaries	Array size (µm)	Array length (mm)
1	50	5	7 x 7	385 x 385	100
2	25	2.5	13 x 13	357 x 357	100
3	10	2	31 x 31	372 x 372	100

The simulation was performed in two parts. The first part deals with 9.17 MeV gamma rays incident on the central capillary and producing electrons / positrons via non-resonant interactions. The second part deals with the interactions of 1.5 MeV protons with the array. These protons are the products of 9.17 MeV gamma rays which interact resonantly with the nitrogen in the scintillator via the photo-nuclear reaction:

$\gamma\ (h\nu\ 9.17\ \mathrm{MeV}) + {}^{14}\mathrm{N}_{g.s.} \rightarrow {}^{13}\mathrm{C}_{g.s.}\ (0.12\ \mathrm{MeV}) + p\ (1.5\ \mathrm{MeV})$

Integration into Geant4 of this reaction cross section is a complicated task which is still ongoing.

4.4.1 Electron tracks

The 9.17MeV gammas are shot at the central capillary, and the simulation tallies the energy deposited in each capillary. The energy is transferred to the scintillator via the gamma ray interactions in the active medium, creating energetic electrons (and a few positrons) that, in turn transfer their energy to scintillations via collisional processes. A better understanding of this behavior can be obtained from the next figure (fig. 31) created in simulation of geometry 1.

In this picture we see the effect of ten gammas shot at the central capillary. Only one of these gammas interacted with the scintillator, via a Compton scattering. As a result, the gamma changed its direction while the associated electron traveled through the array, losing its energy in a series of collisions that excite and ionize the scintillator molecules. When traversing the quartz cladding the electron also loses energy, but does not cause scintillation.

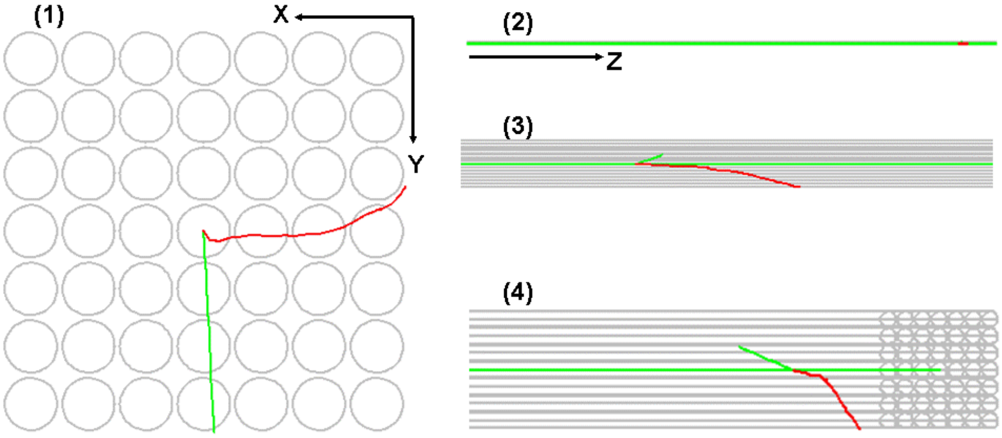

Fig 31: simulation geometry as in fig. 30. (50 µm diameter), results of ten 9.17 MeV gammas shot at the central capillary, one of which creates a single Compton interaction. Green line represents gammas and red line represents electrons. (1) Looking from Z-direction; (2) Z-X plane. This view shows the ratio between length and width of the array. The red spot is the track location; (3) Zoomed view of the track as seen in (2); (4) Rotated and zoomed view of (3). This is a 3D view of the track and array, which emphasizes the track length in comparison to the capillary diameter.

More tracks in the same geometry are presented in Fig. 32 were generated by shooting a larger number (30 and 50) of 9.17 MeV gammas at the central capillary (50 µm diameter capillaries). In these pictures the effects of most possible processes (Compton, Bremsstrahlung, pair production, positron annihilation, etc) are evident.

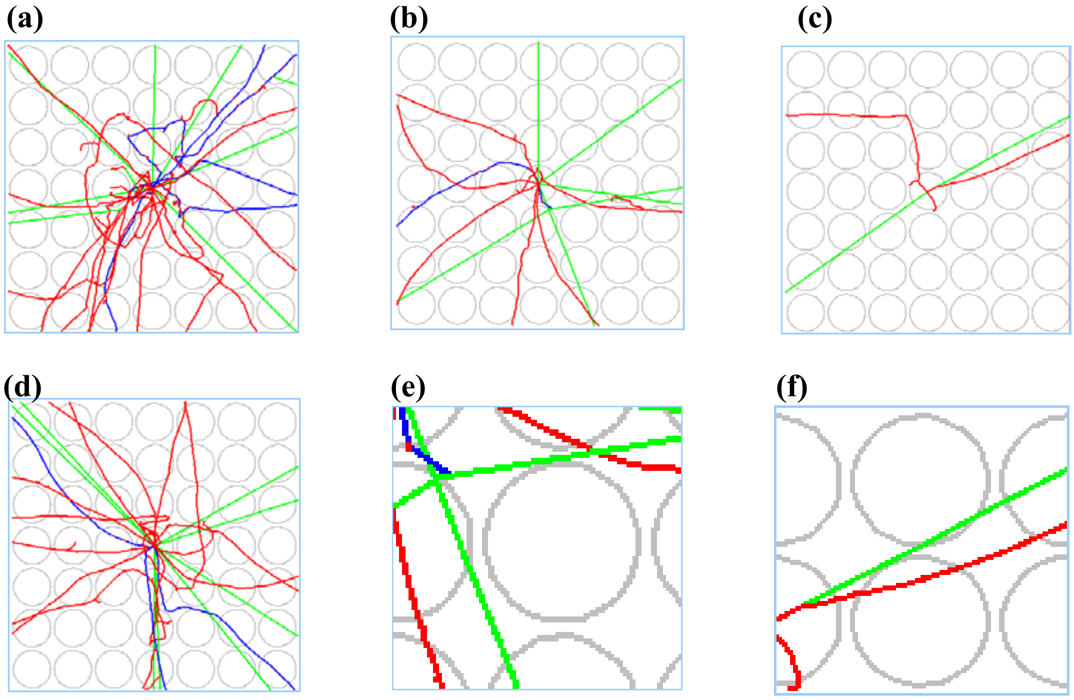

Fig 32: Simulation results of geometry 1 in XY-plane view. The green tracks represent gammas, red tracks represent electrons, and blue tracks represent positrons. . (b), (c) and (a), (d) are pictures of events induced by 30 and 50 gammas shot at the central capillary, respectively. In (b) positron annihilation can be seen, and in (e) a zoomed image of the annihilation is presented. In (c) Bremsstrahlung can be observed at the center capillary, a zoomed image of which is presented in (f).

The tallying convention for energy deposited in a capillary is based on events. An event is defined to include the primary electron created from the gamma and all its delta electrons. The energy deposited in each capillary is summed over all charged particles created in the event.

The logic behind this counting method is that the image obtained in the experimental readout is integrated over long times compared to creation and transit time of all these particles within the scintillating media. Since the readout system has a longer response time than the scintillator – all secondary particles are created within several ns, whereas the experimental readout response takes at least 300 μs. Thus, from the readout point-of-view, the light from an electron and all its descendants is produced simultaneously.

The graphs in Fig. 33, 34, 35 show the result of statistical counting over a large number of events $3X10^5$ gammas) for all three array geometries (1,2, and 3), using this tallying convention. In all three figures, the gammas are shot at the central capillary, represented by graphs (a) – all electron tracks originate in this capillary. Graph (b), (c), (d) in all three figures represents the nearest neighbor and next to nearest neighbor (example geometry is illustrated is in Fig. 36).

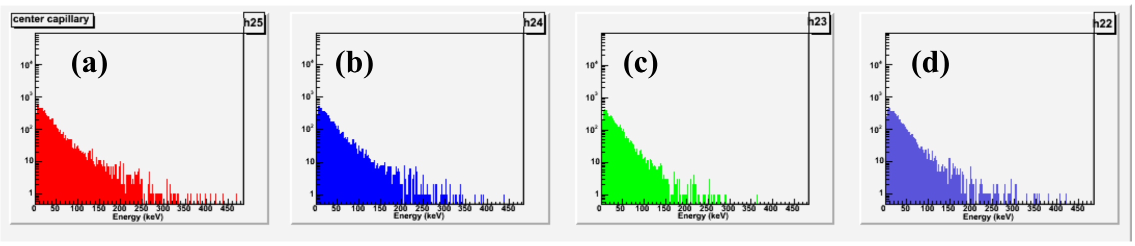

Figure 33: Half a row from 50 µm array – statistical graph. X-axis is energy distribution in keV and the Y- axis is log (number of counts at each energy). This geometry is illustrated in Fig. 30.

In geometries 2 and 3 the line goes on until the 7th capillary in geometry 2 (as illustrated in Fig. 36 and 16th capillary in geometry 3. The energy spectrum of the last capillary in line is illustrated in graphs 34(e), 35(e):

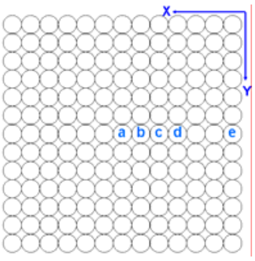

Figure 36: XY plane of geometry 2

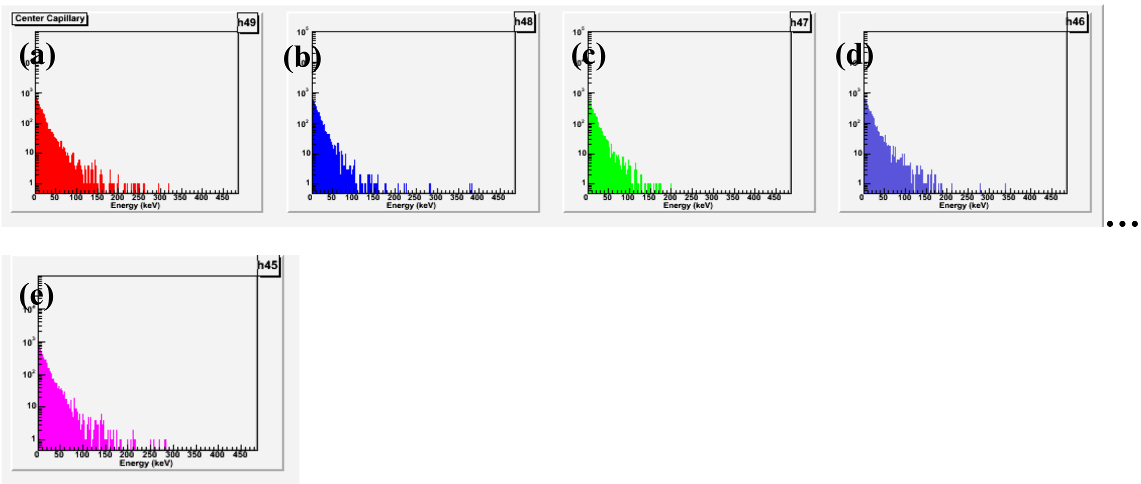

Figure 34: Same as Fig. 33 but for 25 µm diameter capillaries (geometry 2 in Table VII)

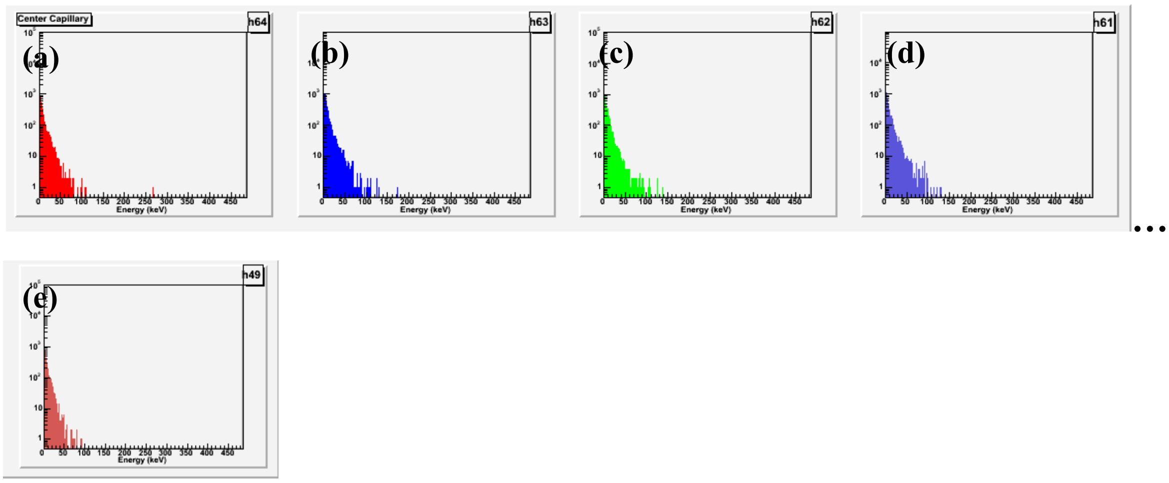

Figure 35: Same as Fig. 34, but for 10 μm diameter capillaries (geometry 3 in Table VII).

In all three array types the average energy deposited in each capillary decreases along the array line – the center capillary (graph (a)) average energy is slightly higher than the energy in the next capillary (graph (b)) and so on. The difference is most evident when comparing the first (graph (a)) and last (graph (e)) capillary in the 10 μm diameter array line (Fig. 34).

Shooting 3x10^5 gammas, ~5x10^4 events were created. The plots show that, on average, a single photon will create a 'cloud' of light from the neighboring capillaries, which is the average of many tracks.

This increases the intensity of the background and renders the separation of proton tracks from electron tracks more difficult. In order to decrease this type of noise, the capillary diameter needs to be reduced, to improve the resolution. Table VIII shows the maximal energies deposited per capillary for all diameters:

Table VIII: Maximal energy deposited by electrons in a single capillary for different capillary diameters.

Diameter (μm)	Maximal energy (keV)
50	400
25	300
10	110

As is evident from this table, the energy deposited by an electron in a single capillary scales with the capillary diameter.

4.4.2 Proton tracks

The reaction responsible for creating protons in the nitrogen-rich liquid scintillator is the photo-nuclear reaction $^{14}N(\gamma,p)^{13}C$. The results of this reaction are 1.5 MeV protons emitted internally to the detector. Single 1.5 MeV protons incident on capillaries filled with liquid scintillator were simulated, but not the (γ,p) reaction that produces them.

At this energy the protons interact both with the scintillator and the quartz cladding via ionization. However, the protons tracks are very short (typically ~50 μm) and they reach the quartz cladding only if they are produced close to it or if the capillary diameter is small enough.

The principal interaction of such protons with the scintillator and the quartz cladding is through ionization. The simulation confirms this, since the correct particle range was obtained (50 μm on average) when ionization was the sole interaction mechanism kept operative.

Protons are slow (comparing to electrons) and their specific energy loss dE/dX is much higher, rendering their track much shorter. Predominantly, the proton will lose all its energy in the capillary it was created in. In Fig. 37 such a simulated track is presented; the blue line represents the proton track and the red dots are secondary low-energy electrons created along its track.

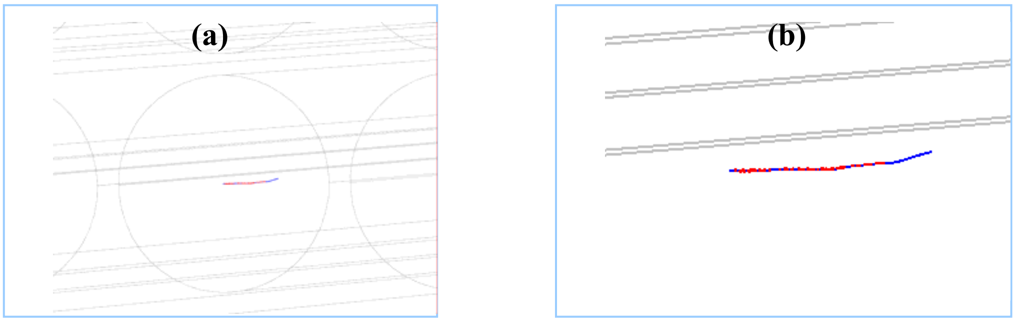

Fig. 37 – Example of 1.5 MeV proton track calculated using ionization processes only. Capillary diameter is 50 μm. (b) is a zoomed view of (a). Gray lines represent the walls of the capillary array in the simulated geometry

For the most part, protons incident in parallel to the principal capillary axis will not migrate from the capillary in which they originated. Simulation results for 10-50 μm are presented in the following Figs. 38, 39, 40. These figures present distributions of the energy that protons deposit in neighboring capillaries (similar to the graphs for electrons in Figs. 33, 34, 35). The left graph in each row is the central capillary, on which 10^6 protons impinged, in parallel to the principal axis. The right graph is the deposited energy distribution in the adjacent capillary. The X-axis represents the energy in keV and the Y-axis the number of counts, on a logarithmic scale.

In all three graphs the protons predominantly deposit all their energy in their original capillary. It is clear from these figures that (as expected) the number of protons migrating from the original capillary to an adjacent capillary increases with as the capillary diameter decreases. But, even in 10 µm capillaries the number of protons migrating to an adjacent capillary is negligible in comparison to the others.

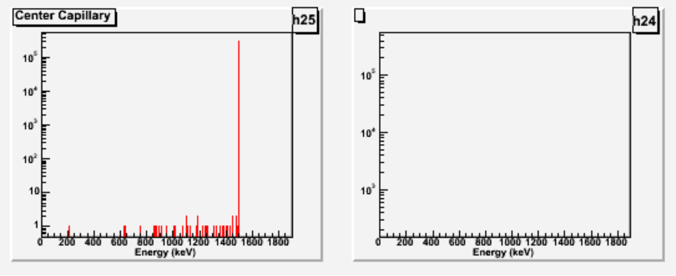

Figure 38: Number of counts (log scale) vs. energy deposited in 50 µm diameter capillaries.

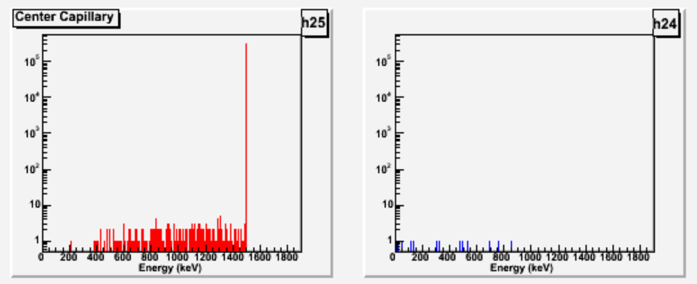

Figure 39: Same as Fig. 38, 25 µm diameter capillaries

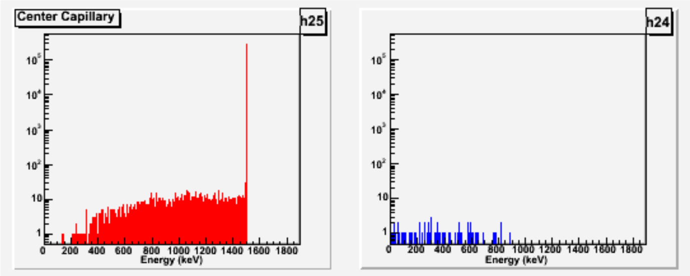

Figure 40: Same as Fig. 38, 10 µm diameter capillaries

In reality, protons are emitted in all directions, not just parallel to the principal capillary axis. The angular distribution of the protons emitted from the $^{14}N(\gamma,p)^{13}C$ reaction is not well known, but presumed to be close to isotropic. A detailed simulation of this reaction and the specific capillary-array configuration and dimensions are required in order to obtain a better estimate of the average number of capillaries a proton would traverse.

One immediate result of the proton track simulations concerns the track broadening effect. In principle, the secondary δ-electrons emitted by the proton along its track could broaden the track, giving rise to some loss of image resolution. However the above simulations show that this effect is confined to the limits of a single capillary, even at diameters as small as 10 μm. The effect is therefore negligible.

4.5 Track-based particle discrimination

Simulating bulk materials, the length and deviation from the original track direction were calculated. Average results over 10^3 primary particles (electrons created from 9.17 MeV gamma rays and 1.5 MeV protons) are presented in Table IX.

Table IX: average track length and deviations from the original track direction. Averaged over 10^3 primary particles: 9.17 MeV γ–rays, 1.5 MeV protons.

particle	Material	Total track length (mm)	Deviation from original particle direction (mm)
electron	scintillator	30	10
electron	quartz	15	5
proton	scintillator	0.051	0.020

The track projection on the XY plane (which is what the readout system will display – see Fig 41), is significant for the discrimination between electron and proton tracks.

For the capillary array used in the Bern experiment (see section 3.2.1) a realistic approximation is that the path-lengths of an electron along its track in the liquid core scintillator and in the quartz cladding are equal. Thus, the average total track length (range) in the capillary array is 22.5 mm. Minimal track length is realized when it is perpendicular to the XY plane.

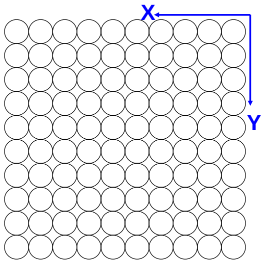

Figure 41: figure repeated for convenience. (a) Fig. 30 from section 4.4.1 – geometry of simulation

The proton average tracks, calculated in the same manner, yield a track projection in the XY plane of 0.020-0.051 mm (20-51 μm). Consequently, 50 μm capillaries definitely allow for a satisfactory electron-proton discrimination.

Much smaller capillary diameters, such as 10 μm, may be sub-optimal – since the protons are emitted quasi-isotropically, a large number of protons will cause scintillation in at least two capillaries along their track. Nevertheless, the pattern will still be very different from electron tracks.

4.6 Future simulations

In attempting to establish the optimal capillary diameter for the GRA application, the simulation needs to take into account all the following:

(a) The average electron and proton energies deposited in all pixels along the tracks

(b) The conversion of these energies to scintillation yields 11)

(c) The light collection process of the entire readout system.

Whereas (a) and (c) are self-explanatory, for (b) it should be borne in mind that the conversion from deposited energy to scintillation light output is not the same for electrons and protons at similar energies because of the different velocity regimes. All the above need to be incorporated in the simulation in order to constitute a realistic calculation of detector efficiency.

5. Summary

The material in this thesis describes three tasks that were performed: developing a suitable scintillator, a first experiment and computer simulations. Together, these constitute a preliminary proof-of-principle study towards a particle detector that is based on a micrometric glass capillary array filled with nitrogen-rich liquid scintillator. This detector is a central part of the Soreq NRC R&D program for explosives detection, based on the GRA method.

The development of the special-purpose high-refractive-index, nitrogen-rich scintillator was fully accomplished. Two nearly equivalent cocktails were produced. The first of these is more readily available and cost-effective, whereas the second exhibits slightly higher light yield (see chapter 2). Both cocktails have excellent light yield, as well as high refractive indices. They thus fulfil all the specified requirements for the scintillator in question. This cocktail was used in the Bern experiment. A further test included dissolving small amounts of NRA in the selected cocktail, to create a first prototype of the ultimate detector.

An experiment was conducted at Bern University (chapter 3) and some promising data collected. Towards this, a prototype capillary detector was assembled, including the associated filling and readout systems. The results show that proton tracks are distinguishable from electron tracks at relevant energies, on basis of a criterion that combines track length and overall light intensity.

The simulations of the detector were designed to provide a better understanding of the processes that take place within it (see chapter 4). The processes and particles were simulated, and calculation of their behavior at various capillary diameters was performed. The results support the phenomena observed in the Bern experiment and account for the particle behavior. An interesting result of the simulations is that proton track-broadening due to δ-electrons has been shown to be negligible, even at diameters as small as 10 μm.

The next stage of the study will require realistic calculation of the optimal capillary diameter for the GRA application. Further simulations will be required, including the conversion of particle energy to scintillation light, the mean energy deposited in an individual capillary by each particle, the light transport along the readout system and a full simulation of the (γ,p) reaction. On the experimental side, an improved generation of the all detector systems, is in the process of being developed at Soreq, on the basis of the all the knowledge and experience obtained so far.

6. Appendices

6.1. Appendix A: Pulse Shape Discrimination (PSD)

For typical organic scintillators the fast fluorescence mechanism of section 1.2.2 is responsible for most of the observed scintillation light yield [11)]. However, longer components corresponding to delayed fluorescence are also observed in many cases. Indeed, the light yield curve can be crudely represented by the sum of two exponential decays, denoted here as the fast and slow scintillation components. The fast component has a decay time of a few ns, but the slow-component decay time is characteristically several hundreds of ns. This slow component, although it is responsible for only a small fraction of the total scintillation yield (typically 10%), has a very useful property: The fraction of light in it depends, in many scintillators on the nature of the exciting particle. It can therefore be used to discriminate between particle types; this is generally known as Pulse-Shape-Discrimination (PSD) [11)].

PSD in the GRA application is employed with the scintillator bulk detectors, the detector technology that preceded the capillary array detectors. The scintillator used in these detectors until now was a modified version of the classical commercial PSD scintillator BC501A (or its forerunner NE213) doped with an inert Nitrogen-rich additive.

The PSD spectra in our Soreq tests were acquired using a ^{241}AmBe source which emits γ-rays and fast neutrons. The neutrons produce knock-on protons in the scintillator; these have light properties similar to those of photo-nuclear protons.

The PSD main figure of merit is the peak-to-valley ratio (P/V) – number of counts at the electron induced peak divided by the minimal 10-channel average in the valley between the γ and n peaks. The distance between the electron peak center and the neutron peak center is another figure of merit – they should be as far apart as possible. In BC501A, P/V = 1000 and distance between peak is ~20 ns, at a threshold discrimination level of ~200 keV

Naphthalene is a well known additive for promoting PSD properties. However, predicting the quantitative effect of Naphthalene concentration on a scintillator PSD is not possible, given the incomplete understanding of the molecular processes involved. Nevertheless, it is generally assumed that the slow component is due to molecules excited to the triplet state. Empirically, the Naphthalene concentration in Soreq's home-made equivalent of BC501A is 7-8% wt/wt.

During the test of the new, high-refractive-index scintillator for the capillary array detector, the PSD properties of the final candidate cocktail were measured with promising results. Systematic tests were not conducted since the PSD properties are irrelevant to the capillary array detector.

New scintillator cocktails tested:

1 – 1MN + 2.5 g/l OG 408

2 – 1MN + 2.5 g/l OG408 + 15 g/l PPO + 5% Naphthalene

3 - 1MN + 2.5 g/l OG408 + 15 g/l PPO + 7.5%, Naphthalene (22.5 ns 1150= P/V)

4 – 1MN + 2.5 g/l bis-MSB + 5 g/l PPO + 5% Naphthalene (15 ns P/V=600)

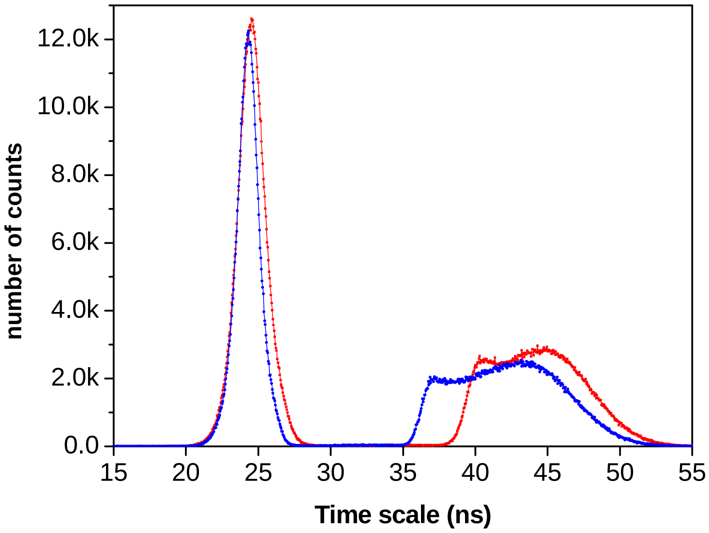

Figure 42: PSD of BC501A (blue) and cocktail 3 (red). The time scale is relative.

The blue spectrum in the graphs is BC501A - the criterion for comparison. The time scale should only be used to calculate relative quantities such as the distance between peaks.

The optimal PSD result is presented in Fig 42 - cocktail 3: P/V = 1150 and 22.5 ns between peaks. Both figures- of merit are significantly superior to those achieved with BC501A. This PSD quality could be utilized to improve the performance of the previous-generation GRA detectors. Cocktails 1, 2 are based on the same components but with different Naphthalene concentrations. Both exhibited PSD properties inferior to those of cocktail 3.

A cocktail containing bis-MSB as phosphor was also measured. The results were less good, as can be seen in Fig. 43.

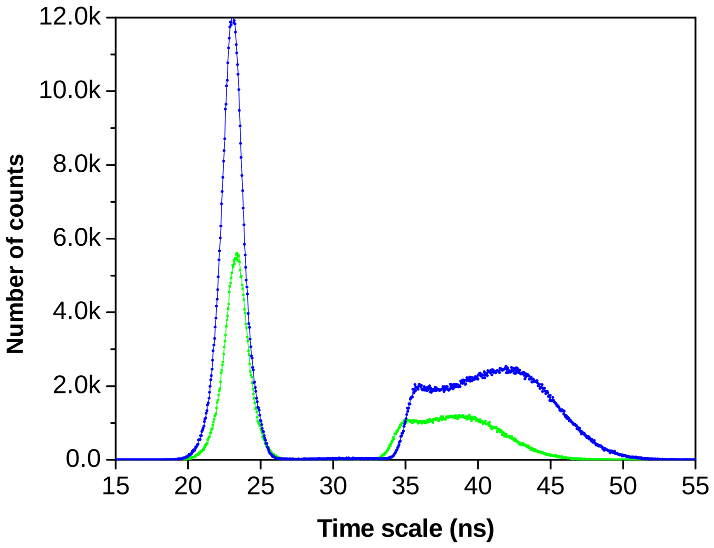

Figure 43: PSD of BC501A (blue) and cocktail bis-MSB – 4 (green). The BC501A data has higher counting statistics. The time scale is relative.

6.2. Appendix B: Light decay times

These curves were measured by Ronald Lauck of PTB, Braunschweig, as part of his PhD thesis (to be published [27)]) and are quoted for completeness in chapter 2.

The light curves show the time-dependent behavior of scintillation light. The light yield curve is represented roughly by the sum of two exponential decays: the fast and slow scintillation components. The fast component has a decay time of several ns but the characteristic decay time of the slow component is up to 1 μs.

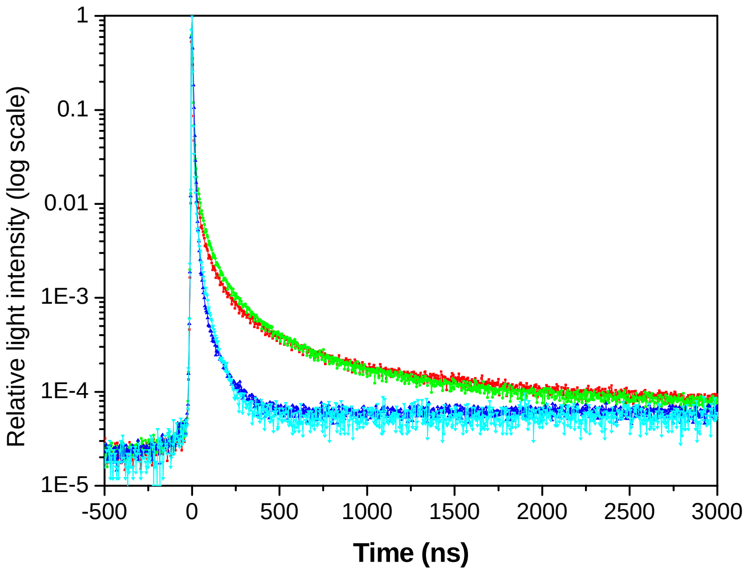

Figure 44: Light decay time curves of interesting scintillators.

(a) —■— 1MN +3 g/l OG408 + 10 g/l PPO, N_2
(b) —●— 1MN +3 g/l OG408 + 10 g/l PPO + NRA, N_2
(c) —▲— 1MN +5 g/l OG408, O_2
(d) —▼— 1MN +3 g/l OG408 + 10 g/l PPO, O_2

The first interesting thing about these curves is that doping with the NRA does not change the time-dependent shape of the scintillator signal. Curves (a) & (b) refer to the same scintillator cocktail, without and with NRA doping, respectively. The undoped scintillator is marginally faster, but the difference is not significant.

Thus, NRA doping attenuates the light signal to the same extent in the fast and slow components. This indicates that it does not attenuate the scintillator light yield by collisional quenching processes, but primarily by competing with the solvent molecules for energy dissipated by the ionizing particle, as an ideal bystander dopant should.

We can also see that this scintillator is rather slow; so that it is not surprising it has good PSD properties (PSD properties rely on the shape of the slow component – appendix A).

The effect of dissolved molecular oxygen on the time dependent behavior of the light can be deduced from comparing graphs (a) and (d).They relate to the same scintillator cocktail with reduced oxygen presence (bubbled with nitrogen, graph (a)) and with high oxygen presence (bubbled with oxygen, graph (d)).

As expected, the presence of oxygen attenuates the slow decay component drastically, whereas the fast component is only moderately affected. The decay of the undoped scintillator exhibits a long component (up to 2 μs) which completely disappears when oxygen is added.

6.3. Appendix C: Correcting for system instability

During the early scintillator light output investigations some instability was detected in the system response. In order to quantify this instability and correct for it as best as we could, a set of tests was conducted.

Examples of tests conducted in this series are presented in Table X. The same sealed NE213 sample was used in all tests to ensure that actual light yield does not vary systematically over the period of the tests.

The tests lasted several days and included heating and cooling of the ambient environment and the PMT tube, varying the room temperature by means of the A/C unit, opening the cover of the light-tight enclosure for different time intervals, etc.

The quantity measured was the channel number in which the Compton peak is located on the multichannel, the energy calibration being 1 keV/channel. This quantity is determined with ±3 channels accuracy. The gamma source f was ^{137}Cs.

The best measured example of the instability is between Run 1 and Run 2. No change was made in the 5 minutes that elapsed between these two measurements, but the pulse height decreased by 52 channels. In contrast, in the 15 minutes that elapsed between Runs 5 and 6 no change was made either and the 2-channel difference is insignificant.

Table X: A selection of the test results, presented in chronological order.

			Variation from previous run.
			waited 5 minutes

			first thing in the morning, room temperature ~30^{o} Centigrade
			Room cooled to ~25^{o}
			25^{o}, after gain had stabilized
			waited 15 minutes
			exposure of PMT to room light for 1 minute

			exposure of PMT to room light for 5 minute
			first thing in the morning, room temperature ~30° Centigrade
			room cooled to ~25°

Cooling room temperature by 5° Centigrade did not affect the gain significantly, as can be seen from comparing runs 4 and 5, and also runs 9 and 10. Exposure of the photomultiplier (PMT) to room light does not affect the channel number significantly either (see runs 6, 7, 8).

No single cause could be isolated as being responsible for the instability, although the PMT was deemed to be the most probable cause. However, the magnitude and range of this instability were determined. Over three days and under varying conditions, the range of the gain instability was 58 channels, corresponding to ±6 % fluctuations. To enhance the reliability of our measurements, the normalization procedure detailed in section 2.4 was devised.

Even though the anode peak voltage as measured in the oscilloscope did not exhibit these fluctuations, the normalization procedure was carried out on this signal as well, in order to eliminate unexpected sources of noise and facilitate the calculations.

6.4. Appendix D: List: scintillator component materials

Abbreviation	**Full name**	**Phase**[*]	**function**	**supplier**
1MN	1-MethylNaphthalene	L	Solvent	Fluka
1PN	1-PhenylNaphthalene	L	Solvent	Aldrich
p-Xylene	Para-Xylene	L	Solvent	Fluka
PPO	2,5-Diphenyloxazole	S	Phosphor	Packard

DMPOPOP	1,4-Bis(4-methyl-5-phenyl-2-oxazolyl)benzene	S	Phosphor	Sigma
POPOP	2,2′-*p*-Phenylene-bis(5-phenyloxazole)	S	Phosphor	Aldrich
OG-408	Sexaphenyl	S	Phosphor	
OG-426	Octiphenyl	S	Phosphor	
TPB	1,1,4,4-Tetraphenyl-1,3-butadiene	S	Phosphor	Fluka
TBP	1,1,4,4-Tetraphenyl-1,3-butadiene	S	Phosphor	Aldrich
TBP	1,1,4,4-Tetraphenyl-1,3-butadiene	S	Phosphor	National Diagnostics
bis-MSB	1,4-Bis(2-methylstyryl)benzene	S	Phosphor	Packard
α-NPO	2-(1-Naphthyl)-5-phenyloxazole	S	Phosphor	Sigma
p-Quaterphenyl	Benzerythrene	S	Phosphor	Aldrich
PPD	2,5-Diphenyl-1,3,4-oxadiazole	S	Phosphor	Sigma

Naphthalene	Naphthalene	S	additive	Packard
2MN	2-MethylNaphthalene	S	Solvent	Fluka
NE213 BC501A	p-xylene + PPO + DMPOPOP	L	commercial scintillator cocktail	Bicron

* State: L- liquid, S- solid crystalline powder

References:

1) D. Vartsky, M.B. Goldberg et al., "Detectors for the gamma-ray resonant absorption method of explosives detection in cargo: A comparative study" Proc. SPIE Int. Soc. Opt. Eng 5198 (2004) 243

2) D. Vartsky, M.B. Goldberg et al., "The total width of the 9.17 MeV level in ^{14}N", Nucl. Phys. A505 (1989) 328

3) D. Vartsky, G. Engler, M.B. Goldberg, "A method for detection of explosives based in nuclear resonance absorption of gamma rays in ^{14}N", Nucl. Instr. & Meth. A348 (1994) 688

4) M.B. Goldberg, D. Vartsky et al., "Nuclear resonance absorption: Method and application to detection of contraband in baggage, cargo and vehicles", IAEC-annual report (1994) 52

5) M.B. Goldberg, D. Vartsky et al., "Improved Nitrogen-Rich Detectors and Data-Normalization Procedures for a Gamma-Resonance-Absorption (GRA)-Based Cargo

Container EDS", Technical reports 1,2,3 to Transportation Security Labratories (TSL), 2006-2007

6) F.R. Metzger, "Resonance Fluorescence in Nuclei", In Prog. in Nucl. Phys. Vol. 7 54-88 (ed. O.R. Frisch, Pergamon Press, 1959)

7) J.B. Birks, "The theory and Practice of scintillation counting", (Pergamon Press 1964)

8) L. Michel, "Study of properties of liquid organic scintillators", PhD Thesis, Univ. Catholique de Louvain (1995).

9) P. Annis et al., "High-resolution tracking using large capillary bundles filled with liquid scintillator", Nucl. Instr. & Meth. A449 (2000) 60 & refs. therein

10) Kai Siegbahn, "Alpha-Beta-and gamma-ray spectroscopy", (N.H. 1965)

11) G.F. Knoll, "Radiation detection and measurements", (John Wiley Inc. 2000)

12) P. Annis et al., "Tracking with capillaries and liquid scintillators", Nucl. Phys. B 61B (1998) 390

13) P. Annis et al., "A new vertex detector made of glass capillaries", Nucl. Instr. & Meth. A386 (1997) 72

14) J. Konijn et al., "Capillary detectors", Nucl. Instr. & Meth. A418 (1998) 186

15) R.P Feynman, "The Feynman lectures on physics", Vol. II (Addison-Wesley ,1964)

16) C.P. Achenbach, A.G. Cobb, "Computational studies of light acceptence and propagation in straight and curved multimodal active fibers", J. Opt. A: Pure Appl. Opt. 5 (2003) 239

17) "Geant4 simulation toolkit user's guide: For application developers", http://geant4.web.cern.ch/geant4/

18) "Geant4 Physics reference guide", http://geant4.web.cern.ch/geant4/

19) I.B. Berlman, "Handbook of Fluorescence Spectra of Aromatic Molecules", (Acad. Press, 1971).

20) S.V. Golovkin et al., "New liquid scintillators for particle detectors based on capillary fibers", IHEP Preprint 96-13 (1996)

21) S.W. Wunderly and J.M. Kauffman, "New quench-resistant flours for liquid scintillation counting", Int. J. Radiat. Appl. Instrum. Part A 41 (1990) 809.

22) J.M. Kauffman et al., "Electronic absorption and emission spectral data and fluorescence quantum yields of bridged p-oligophenylenes, bi- to deciphenyls, and related furans and carbazoles", J. of Fluorescence 5 (1995) 295.

23) G.I. Britvich et al., "Scintillating properties of frozen new liquid scintillators", Nucl. Instr. & Meth. A425 (1999) 498

24) S Buontempo et al., "Influence of dissolved gas and temperature on the light yield of new liquid scintillators", Nucl. Instr. & Meth. A425 (1999) 492

25) H.R.V. Carrillo, "Neutron and gamma ray spectra of ^{239}PuBe and ^{241}AmBe", Int. J. Appl. Rad .& Isot. 57(2002) 167

26) J.F. Janni, "Proton Range-Energy Tables, 1 keV – 10 GeV", Atomic Data & Nucl. Data Tables, 27 (1982) 341.

27) Ronald Lauck (PTB-Braunschweig), private communication